

1 Deforestation as an anthropogenic driver of
2 mercury pollution

3 *Aryeh Feinberg^{a*}, Martin Jiskra^{b*}, Pasquale Borrelli^c, Jagannath Biswakarma^{b,d}, and*
4 *Noelle E. Selin^{a,e}*

5 ^a Institute for Data, Systems, and Society, Massachusetts Institute of Technology,
6 Cambridge, MA, USA

7 ^b Environmental Geosciences, University of Basel, Basel, Switzerland

8 ^c Department of Science, Roma Tre University, Rome, Italy

9 ^d Department of Water Resources and Drinking Water, Eawag, Dübendorf, Switzerland

10 ^e Department of Earth, Atmospheric, and Planetary Sciences, Massachusetts Institute of
11 Technology, Cambridge, MA, USA

12 *Correspondence to: arifeinberg@gmail.com (A.F.); martin.jiskra@gmail.com (M.J.)

13

14 **KEYWORDS.** Mercury, deforestation, land use change, emissions, Minamata
15 Convention, Amazon rainforest, reforestation, chemical-transport modeling.

16

17 **Abstract**

18 Deforestation reduces the capacity of the terrestrial biosphere to take up the toxic heavy
19 metal mercury (Hg) and enhances the release of secondary Hg from soils. The
20 consequences of deforestation for Hg cycling are not currently considered by
21 anthropogenic emissions inventories or specifically addressed under the global Minamata
22 Convention on Mercury. Using global Hg modeling constrained by field observations, we
23 estimate that net atmospheric Hg fluxes due to deforestation are 217 Mg yr^{-1} (95%
24 confidence interval, CI: $134\text{--}1650 \text{ Mg yr}^{-1}$) for 2015, approximately 10% of global
25 primary anthropogenic emissions. If deforestation of the Amazon rainforest continues at
26 business-as-usual rates, net Hg emissions from the region will increase by 153 Mg yr^{-1} by
27 2050 (CI: $97\text{--}418 \text{ Mg yr}^{-1}$), enhancing the transport and subsequent deposition of Hg to
28 aquatic ecosystems. We calculate the potential for substantial Hg emissions reductions
29 for two cases of land use policies: conservation of the Amazon rainforest (92 Mg yr^{-1} , CI:
30 $59\text{ to }234 \text{ Mg yr}^{-1}$) and global reforestation (98 Mg yr^{-1} , CI: $64\text{ to }449 \text{ Mg yr}^{-1}$). We
31 conclude that deforestation-related emissions should be incorporated as an anthropogenic
32 source in Hg inventories, and that land use policy could be leveraged to address global
33 Hg pollution.

34 **Synopsis**

35 Deforestation is an overlooked source of Hg to air and water. This study quantifies the
36 global fluxes of Hg due to deforestation and investigates the impacts of policies to
37 mitigate these fluxes.

38

39 *Main Text*

40 **Introduction**

41 Humans are exposed to the organic form of mercury (Hg), methylmercury (MeHg),
42 mainly through seafood consumption¹. Methylmercury is a potent neurotoxin, impairing
43 the neurodevelopment of fetuses and children and costing the global economy \$20–117
44 billion annually according to some estimates^{2,3}. Mercury is emitted to the atmosphere by:
45 a) primary anthropogenic sources, including artisanal and small-scale gold mining
46 (ASGM), fossil fuel combustion, and metal smelting; b) re-emissions of historical
47 anthropogenic (“legacy”) Hg from ocean and land; and c) geogenic sources⁴. Mercury
48 spreads globally in the atmosphere due to its long lifetime against deposition of 4–6
49 months⁵. A global treaty, the Minamata Convention on Mercury, aims to protect human
50 health and the environment from anthropogenic emissions and releases of Hg. The
51 Convention’s measures target primary anthropogenic emissions sources by phasing out
52 Hg use and adopting best available technologies for pollution control⁶. However, primary
53 anthropogenic emissions account for only 30% of present-day total emissions, with
54 legacy re-emissions from land and ocean accounting for 60% ⁷. The future of Hg
55 pollution will depend not only on reducing direct emissions through the Minamata
56 Convention, but also on indirect anthropogenic influences on legacy Hg emissions and
57 fate.

58 Terrestrial ecosystems, and especially forests, are important sinks of Hg from the
59 atmosphere, taking up an estimated 2200–3600 Mg Hg per year⁸, more than a third of
60 total (anthropogenic, legacy, and geogenic) Hg emissions (7400 Mg yr⁻¹)⁹. By taking up
61 Hg, terrestrial ecosystems reduce the burden of Hg depositing in oceans and freshwater
62 systems, where it can be converted to MeHg and bioaccumulated in fish. Previous studies
63 have drawn useful analogies between Hg and carbon cycling in terrestrial ecosystems^{10,11}.
64 Like carbon dioxide (CO₂), elemental mercury (Hg⁰) is assimilated by foliage throughout
65 the growing season¹². Mercury is transported from the canopy to soil by foliage falling to
66 the ground (“litterfall”) and dry deposited Hg being washed off by precipitation
67 (“throughfall”), which together are the major source (60–90%) of Hg in soils⁸.
68 Anthropogenic land use and land cover changes (LULCC), including deforestation,

69 perturb both CO₂ and Hg fluxes to the atmosphere¹³⁻¹⁵. In the case of carbon, scientific
70 assessments¹⁴ have calculated the contribution of LULCC to total anthropogenic CO₂
71 emissions (13% of total), and land management practices are governed by Article 5 of the
72 Paris Agreement¹⁶. For Hg, on the other hand, quantitative estimates of the overall
73 importance of land cover change are limited. Only one previous study modeled the
74 impact of future LULCC on atmospheric Hg cycling, focusing on the effects of climate-
75 induced changes to vegetation¹⁵. No anthropogenic Hg emissions inventories have
76 quantified the impacts of historical and future deforestation, and land management is not
77 currently addressed by Hg policy efforts like the Minamata Convention.

78 Several processes mobilize Hg from terrestrial systems after deforestation. Along with
79 removing a strong atmospheric sink of Hg⁸, deforestation leads to more insolation
80 reaching the soil, which increases volatilization of Hg from soils through enhanced
81 microbial¹⁷ or photochemical¹⁸ reduction. Fire-mediated deforestation leads to direct
82 emission of Hg from forest and soil biomass¹⁹. Soils in deforested areas are subject to
83 accelerated erosion rates, enhancing Hg export to downstream ecosystems^{17,20,21}. Direct
84 measurement of deforestation-driven fluxes at larger scales is challenging given
85 variations in the land sink due to trends in environmental conditions, necessitating the use
86 of models to quantify these fluxes²². Models of terrestrial–atmosphere Hg fluxes, while
87 still much more uncertain than analogous carbon cycle models, are improving due to a
88 better process understanding and increasing availability of terrestrial
89 measurements^{8,12,23,24}. Thus, the time is ripe for assessing the relative importance of
90 deforestation-driven fluxes in the Hg cycle.

91 Policies on local, national, and international scales will shape the future evolution of
92 deforestation Hg fluxes. Deforestation due to agricultural land conversion threatens the
93 Amazon rainforest^{25,26}, which currently contributes 29% of the global land sink for
94 atmospheric Hg⁰ (ref. ²³). At current deforestation rates, 40% of the Amazon rainforest
95 could be lost by 2050, while enhanced environmental legislation (e.g., expansion of
96 protected areas and enforcement) can reduce the deforested area to 15% (ref. ²⁷).
97 Reforestation and afforestation on the global scale are being studied as part of the
98 solution to reach net zero greenhouse gas emissions in the future²⁸, though the efficacy of

99 these measures has been debated²⁹. In any case, the climate mitigation benefits of
100 forestation would not be realized without accompanying aggressive CO₂ emissions
101 reductions^{29,30}. Similarly, forest conservation and reforestation policies may have
102 potential benefits for Hg sequestration on land, yet the magnitude of impacts remain
103 unquantified.

104 Here, we apply the GEOS-Chem Hg model²³ to calculate deforestation emission factors
105 for Hg from different regions and evaluate them against available observations. We
106 quantify the global atmospheric Hg fluxes in 2015 that result from deforestation (217 Mg
107 yr⁻¹; 95% confidence interval, CI: 134–1650 Mg yr⁻¹). We study the impact of future
108 Amazon deforestation policy scenarios²⁷ and potential global reforestation efforts³⁰ on the
109 terrestrial Hg sink. The magnitude of potential emissions reductions from Amazon
110 conservation (92 Mg yr⁻¹; CI: 59–234 Mg yr⁻¹) and global reforestation (98 Mg yr⁻¹; CI:
111 64–449 Mg yr⁻¹) highlights the importance of land management policies for curbing Hg
112 pollution.

113 **Materials and Methods**

114 *Atmospheric Hg model (GEOS-Chem) description.* In this study, we use the chemical-
115 transport model GEOS-Chem v12.8.1 with Hg⁰ dry deposition updates from Feinberg et
116 al.²³. The global model is run at 2.0° × 2.5° horizontal resolution and 47 vertical layers up
117 to 80 km altitude. The model tracks emissions, transport, chemistry, and deposition of Hg
118 in three chemical tracers: elemental mercury (Hg⁰), oxidized mercury (Hg^{II}), and
119 particulate-bound mercury (Hg^P). Atmospheric transport of Hg species is based on
120 MERRA-2 reanalysis meteorological data³¹. The Hg chemical mechanism assumes that
121 Br is the primary Hg⁰ oxidant and uses offline monthly maps of previously-calculated
122 oxidant concentrations to drive chemistry³². The aqueous photoreduction rate of Hg^{II} to
123 Hg⁰ is parametrized as a function of the organic aerosol concentration and the NO₂
124 photolysis rate³².

125 The wet removal of oxidized Hg (Hg^{II} and Hg^P) from the atmosphere is calculated in
126 online parametrizations considering large-scale and convective scavenging of gas and
127 particulate species³³. Dry deposition in GEOS-Chem applies a resistance-based

128 approach³⁴, which determines the dry deposition velocities depending on meteorology
 129 (e.g., temperature and windspeed), land surface parameters (e.g., land type and leaf area
 130 index, LAI), and compound-specific parameters (biological reactivity, f_0 , and solubility,
 131 H^*). For Hg^0 , f_0 is set to 0.2 within the Amazon rainforest and 3×10^{-5} elsewhere, which
 132 was found to yield the best agreement with available measurements of Hg^0 vegetation
 133 uptake²³. The solubility of Hg^0 is low ($H^* = 0.11 \text{ M atm}^{-1}$), whereas gaseous Hg^{II} is
 134 assumed to be highly soluble ($H^* = 10^{14} \text{ M atm}^{-1}$) and biologically unreactive ($f_0 = 0$).
 135 Dry deposition of Hg^{P} is determined according to the aerosol deposition parameterization
 136 in GEOS-Chem³⁵. Dry deposition is calculated separately over each land type within a
 137 grid cell (e.g., rainforest, grassland, cropland, etc.) and then an overall area-weighted
 138 average is calculated for the grid cell. GEOS-Chem accounts for 73 land types based on
 139 the Gibbs³⁶ land cover product. The LAI data for this study is taken from a reprocessed
 140 version of the Moderate Resolution Imaging Spectroradiometer (MODIS) satellite
 141 product³⁷.

142 Anthropogenic Hg emissions follow AMAP/UNEP estimates³⁸ for 2015. Biomass
 143 burning emissions are taken from the Global Fire Emissions Database (GFED) v4.1s³⁹.
 144 We use fixed concentrations of Hg^0 in the surface ocean based on the MITgcm 3-D ocean
 145 model³² to calculate the Hg^0 air-sea exchange⁴⁰. We adopted a new formulation⁴¹ for the
 146 soil Hg^0 emissions parametrization (Supplementary Information, Section S1):

$$147 \quad E_{\text{soil}} = aC^bR_g^c \quad (\text{Eq. 1})$$

148 where E_{soil} is the Hg^0 emissions from soil (units $\text{ng m}^{-2} \text{ h}^{-1}$), C is the concentration of Hg
 149 in soils, R_g is solar radiation flux at the ground, and a , b , and c , are coefficients (set to 71,
 150 2.5, and 0.76, respectively). We have tuned the coefficients of this parametrization to
 151 match available soil emissions measurements (Section S1). The soil concentration map of
 152 Hg (C) was calculated using the method of Selin et al.⁴², deriving the spatial distribution
 153 of soil concentrations by first assuming a steady state balance between land emissions
 154 and deposition in the preindustrial and subsequently increasing soil concentrations
 155 according to the distribution of anthropogenic Hg deposition. As in Selin et al.⁴², the solar

156 radiation at ground (R_g) is determined by considering attenuation of the solar radiation
 157 flux (R_S) by shading from the overhead canopy, parametrized by the LAI:

$$158 \quad R_g = R_S \exp\left(-\frac{\alpha \text{LAI}}{\cos\theta}\right) \quad (\text{Eq. 2})$$

159 where $\alpha = 0.5$, assuming extinction from a random angular distribution of leaves⁴³, and θ
 160 is the solar zenith angle. We have also updated GEOS-Chem to calculate soil emissions
 161 at the sub-grid scale for each land use category contained within the grid cell.

162 **Reference (HIST) simulation.** We ran a GEOS-Chem simulation for the land cover and
 163 LAI conditions of the year 2003 (HIST simulation), the first year where reprocessed LAI
 164 data is available. To highlight the role of land cover changes alone, we keep
 165 meteorological conditions constant by running all simulations with meteorology for
 166 2014–2015. We consider the first year as spinup to equilibrate the new land cover
 167 conditions, and analyze simulation differences for the meteorological year 2015.

168 **Estimating historical global deforestation-driven Hg emissions.** We calculate regional
 169 emissions factors (EFs) for deforestation through conducting perturbation experiments in
 170 GEOS-Chem. We distinguish emission factors for the following regions based on
 171 biogeographic realms⁴⁴ or specific Hg-relevant characteristics: Palearctic, Nearctic,
 172 Afrotropic, Neotropic, Australasia & Oceania, Indomalaya, China, and the Amazon
 173 rainforest (mapped in Fig. S5). For each region, we conduct a simulation where we
 174 perturb the land cover in grid cells that experience deforestation during 2000–2014 in the
 175 $0.25^\circ \times 0.25^\circ$ resolution CMIP6 Land-Use Harmonization (LUH2) dataset⁴⁵. For these
 176 grid cells, we replace forest land cover with the most common agricultural land cover
 177 relevant to the region: “Crops and Town” (Afrotropic, Indomalaya, Palearctic,
 178 Australasia & Oceania, and China), “Corns and Beans Croplands” (Neotropic and
 179 Nearctic), and “Fields and Woody Savannah” (Amazon). For the new agricultural areas,
 180 the LAI is set to the average annual cycle for the existing agricultural grid cells within the
 181 region. We run 8 deforestation (DFR) simulations (1 for each region) over 2014–2015,
 182 comparing year 2015 fluxes to the HIST simulation. To calculate the net emissions factor

183 (EF) from deforestation, we calculate changes to the land-air exchange over the
 184 deforested grid cells:

$$185 \quad EF = \frac{(E_{DFR} - D_{DFR}) - (E_{HIST} - D_{HIST})}{A_{DFR}} \quad (\text{Eq. 3})$$

186 where E refers to Hg emissions, D refers to Hg deposition, and A refers to the area that is
 187 deforested in the simulation. The emissions factor represents the net emissions of Hg
 188 released by a deforested area annually, in units $\text{Mg m}^{-2} \text{ yr}^{-1}$. The assumption of linearity
 189 of the net emissions to deforested area holds over simulations conducted in the Amazon
 190 with differing spatial distributions of deforestation (Fig. S4), supporting an emissions
 191 factor approach to deforestation. We compared calculated emissions factors with existing
 192 estimates from observational studies^{18,21,24,46–62} for total deforestation EFs and the
 193 component of EFs due to soil Hg^0 emissions (Supplementary Information, Section S2).
 194 Based on our literature review (SI Spreadsheet), observational data is available for three
 195 of the tested regions (Amazon, China, and Nearctic).

196 We apply the regional emissions factor to historical land use data from the LUH2 dataset
 197 to calculate emissions from deforestation. We define gross deforested areas from the
 198 LUH2 dataset by summing the areas with transitions from primary or secondary forest to
 199 a non-forest land type. This approach does not consider LULCC fluxes due to harvesting
 200 of a forest without complete deforestation or the regrowth of vegetation after clearing,
 201 due to a lack of corresponding observations for Hg to constrain these parameters.
 202 Likewise, the emissions factors are assumed to be constant over time, so a deforested area
 203 continues to have the same annual emissions over the considered time horizon. In reality,
 204 deforested areas could have a recovery timescale as vegetation regrows, which is
 205 accounted for in carbon LULCC fluxes⁶³; for Hg, the response timescales during
 206 regrowth are largely unknown. To account for these uncertainties, we produce global and
 207 country-level estimates of Hg emissions in 2015 due to deforestation by summing
 208 deforestation over different time horizons: 15 years (2000–2014), 30 years (1985–2014),
 209 45 years (1970–2014), and 60 years (1955–2014). We present the 45-year (1970–2014)
 210 accumulated results in the main text, with the others presented in Fig. S6.

211 *Future Amazon deforestation scenarios.* We employ deforestation scenarios from
212 Soares-Filho et al.²⁷, who developed a model for predicting the extent of deforestation
213 within the Amazon based on environmental policies and highway construction. They
214 presented two scenarios for 2050, encompassing a range of future deforestation
215 trajectories. In the Business as Usual (BAU) scenario, recent deforestation trends
216 continue into the future, assuming that compliance with conservation laws remains low
217 and no new areas will be protected. On the other hand, the Governance (GOV) scenario
218 assumes the expansion of environmental legislation and increased enforcement of
219 protected areas will lead to a reduction in the deforestation rate. Compared to the
220 Amazon forest area in 2003 (5.3 million km²), in 2050 the BAU scenario projects 3.2
221 million km² remaining and GOV projects 4.5 million km² remaining²⁷. We focus our
222 analysis on comparing the forest coverage in the years 2003 and 2050.

223 We translated these scenarios into required inputs for the calculations in GEOS-Chem
224 (spatially gridded land use categories, LAI, and biomass burning emissions). The Soares-
225 Filho et al.²⁷ dataset assigns 1 km² pixels within the Amazon basin as being forested,
226 deforested, or agricultural areas for every year between 2003 and 2050. We regridded
227 these annual datasets to 0.25° × 0.25° resolution, the native resolution of land use and
228 LAI maps in GEOS-Chem. We calculated the relative change in forested area in the
229 scenarios for every 0.25° × 0.25° grid cell. The rainforest land use category in deforested
230 grid cells is correspondingly reduced by this factor, with the lost land area added to the
231 land use category for “Fields and Woody Savanna”. The LAI annual cycle for existing
232 Fields and Woody Savanna grid cells within the Amazon basin was spatially averaged
233 over 2003 and assigned to the deforested areas. Annual average LAI maps for the
234 Amazon scenarios used in GEOS-Chem are shown in Fig. S9. For these simulations, we
235 assume that conversion of forest to agricultural land within the Amazon is fire-
236 mediated⁶⁴. Gridded biomass burning emissions are calculated by multiplying the newly
237 deforested areas for each year by mean fire Hg emissions (380 μg m⁻² yr⁻¹) from two
238 observational studies in the Amazon^{19,65}. An additional 50% of the emissions (190 μg m⁻²
239 yr⁻¹) are released to the atmosphere within the first year as post-burn Hg⁰ emissions from
240 soils¹⁸. To account for seasonal differences in meteorology and realistic timing for forest

241 clearing and burning⁶⁴, we assumed that deforestation occurs at the start of June and
242 deforestation biomass burning emissions occur in August and September .

243 The BAU and GOV scenarios do not account for any land-climate feedbacks²⁷, wherein
244 deforestation of the rainforest can lead to reduced moisture recycling and widespread
245 *savannization* (conversion of rainforest to savanna)⁶⁶. As an upper bound for this process,
246 we consider an extreme scenario (SAV) where the Amazon rainforest is fully converted
247 to savanna⁶⁷. The impact of this scenario on Hg⁰ deposition was previously quantified²³,
248 but here we reran the SAV simulation in GEOS-Chem to account for updates in the soil
249 Hg⁰ emissions parametrization. In the analysis of results, we calculate fluxes for the
250 Amazon region, averaging over the area covered by the Soares-Filho et al.²⁷ deforestation
251 projections (shown in Fig. S8).

252 ***Potential reforestation scenario.*** We apply a reforestation scenario (RFR) in GEOS-
253 Chem based on the Global Reforestation Potential map^{30,68}, which considers the binary
254 potential of every 1 km² grid cell to be converted from non-forest (<25% tree cover in
255 2000–2009) to forest (>25% tree cover). The reforestation potential dataset does not
256 include areas that are native non-forest land cover types (e.g., grasslands) or cropland
257 areas. We regridded the reforestation potential to 0.25° × 0.25° resolution. For every grid
258 cell where reforestation can occur, we identify the corresponding biome in the
259 Ecoregions2017 dataset⁴⁴ to determine the type of native forest vegetation that would
260 occur. If the corresponding biome of the grid cell is not a forest (e.g., coastal grid cells),
261 we identify the most common forest type in the 8 neighboring grid cells. The added forest
262 is assumed to have a LAI annual cycle equal to the 2003 spatial average for all grid cells
263 in the corresponding biome and biogeographic realm (LAI_{biome}). For grid cells that are not
264 a forest land type in 2003, we convert the reforested area fraction (f_{fr}) from the original
265 land type to the new forest land type. We only reforest grid cells in the case where
266 LAI_{biome} is larger than the original land type LAI (LAI_{old}). Since the land map used in
267 GEOS-Chem is at coarser resolution (0.25° × 0.25°) than the reforestation potential
268 dataset (1 km × 1 km), the reforested grid cell may already be a forest land type in
269 GEOS-Chem. In this case, we assume that the grid cell LAI (LAI_{new}) will become denser
270 due to the new reforested area:

271
$$\text{LAI}_{\text{new}} = \text{LAI}_{\text{old}} + f_{\text{rfr}} \cdot \text{LAI}_{\text{biome}} \quad (\text{Eq. 4})$$

272 The resultant average LAI map in the RFR scenario is shown in Fig. S10.

273 **Uncertainty analysis.** We employ offline Python-based models for Hg^0 dry deposition
274 and soil Hg^0 emissions to estimate uncertainties in the simulated terrestrial-atmosphere
275 Hg fluxes from GEOS-Chem. These models are made publicly available for further reuse
276 (see Code and Data Availability). We focus on offline modeling of the Hg^0 dry
277 deposition and soil emissions as these processes contribute the overwhelming majority
278 (>98%) of the flux response to deforestation. The offline models were run for the year
279 2015 using monthly average diurnal cycles ($12 \times 24 \text{ h} = 288$ timesteps) of meteorological
280 parameters, land surface parameters, and Hg^0 concentration fields. At this time
281 resolution, the offline models show sufficient accuracy compared to full GEOS-Chem
282 simulations, with maximum errors compared to online predictions of 1% for annual mean
283 soil emissions and 5% for Hg^0 deposition. Given this level of accuracy and reduced
284 computational expense, the offline models are appropriate for estimating the parametric
285 uncertainties in atmosphere-terrestrial fluxes of the online GEOS-Chem model. We
286 consider the contributions of deposition parameters, soil emission parametrizations, the
287 assumption for LAI for replaced land types, and biomass burning emission factors (for
288 the Amazon simulations) to the overall uncertainty in fluxes. Uncertainty bounds of these
289 parameters are tabulated in Table S4. We sample 100 parameter combinations using
290 Latin Hypercube sampling⁶⁹. We conducted 100 simulations in the offline emissions and
291 deposition models for each studied scenario, calculating 95% confidence intervals from
292 the 2.5th and 97.5th percentile values in the offline calculated fluxes.

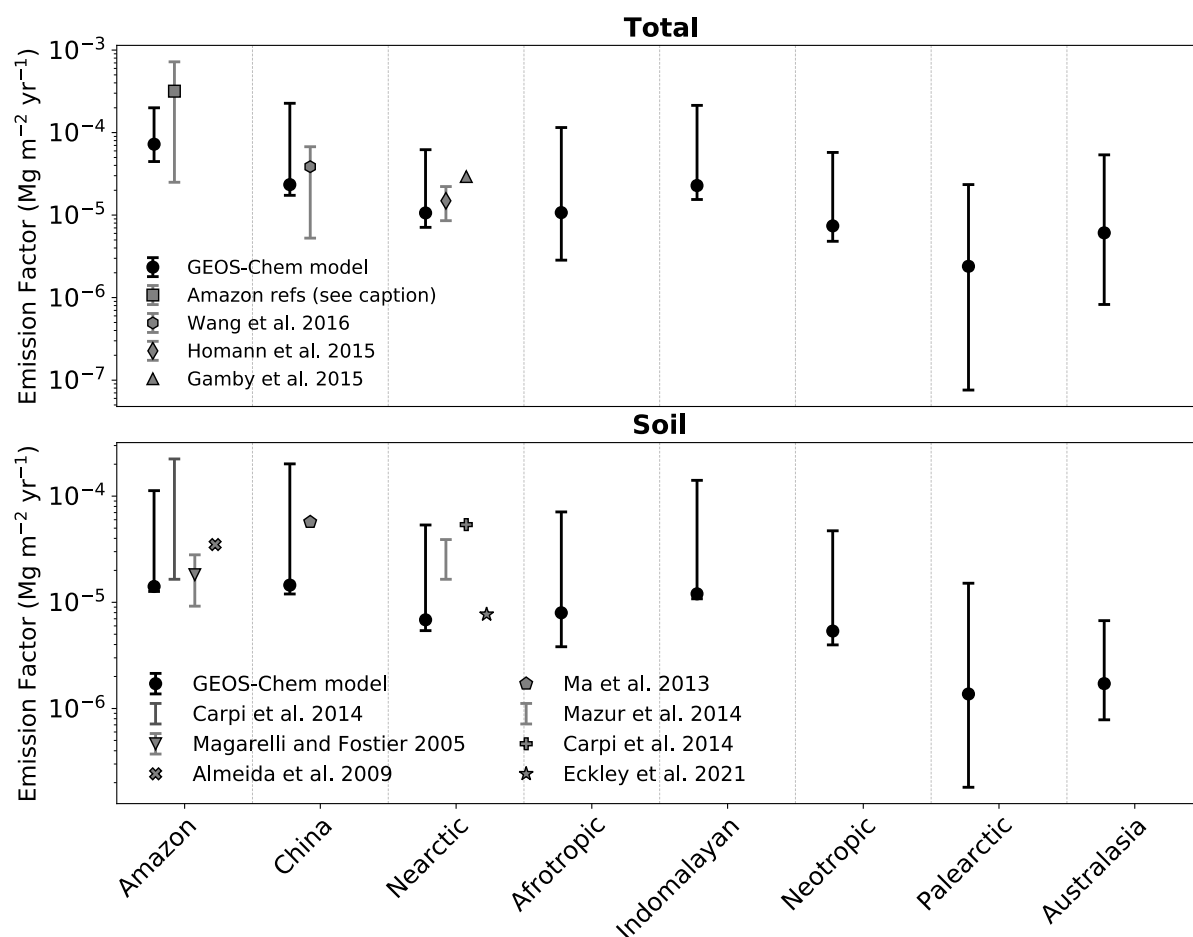
293

294 **Results and Discussion**

295 **Global estimate of deforestation-driven Hg fluxes.** In quantifying changes to Hg fluxes
296 after deforestation, we define the net deforestation emissions as the change in the net
297 terrestrial-atmosphere exchange (emissions minus deposition) over a deforested area. For
298 our global estimate of deforestation-driven emissions, we do not consider immediate
299 biomass burning emissions of Hg due to fire-mediated forest clearing nor enhanced

300 erosion fluxes, instead focusing on the impact on net Hg fluxes to the atmosphere in the
301 years after the clearing event. The major impacts to Hg fluxes arise through enhanced soil
302 Hg⁰ emissions and decreased Hg⁰ dry deposition due to reduced canopy coverage, which
303 can continue many years after the initial deforestation event^{18,59}. Using perturbation
304 simulations in GEOS-Chem for 8 global land regions, we calculated regional emission
305 factors (EFs) representing net fluxes to the atmosphere per unit deforested area (in units
306 Mg Hg m⁻² yr⁻¹).

307 The calculated EFs are on the order of 10⁻⁶ to 10⁻⁴ Mg Hg m⁻² yr⁻¹ depending on the
308 region (Fig. 1; Table S3), with the Amazon rainforest showing the highest EF (7×10^{-5}
309 Mg Hg m⁻² yr⁻¹; CI: 4×10^{-5} to 2×10^{-4} Mg Hg m⁻² yr⁻¹). This is to be expected from
310 litterfall and throughfall measurements in the Amazon, which show some of the highest
311 levels of Hg⁰ vegetation uptake observed globally¹³, as well as Hg⁰ soil flux
312 measurements from deforested areas in the Amazon, which show higher levels of
313 emissions compared to deforested North American soils¹⁸. We compiled available
314 estimates of deforestation EFs from previous observational studies^{18,21,24,46-62} and
315 compare these to our modeled values (Fig. 1). Our EFs overlap with available factors
316 derived from observations, for the three regions where data are available. The modeled
317 error ranges appear well-calibrated as they cover a similar range as the variability
318 between observation-derived fluxes in the same region (Fig. 1).



319

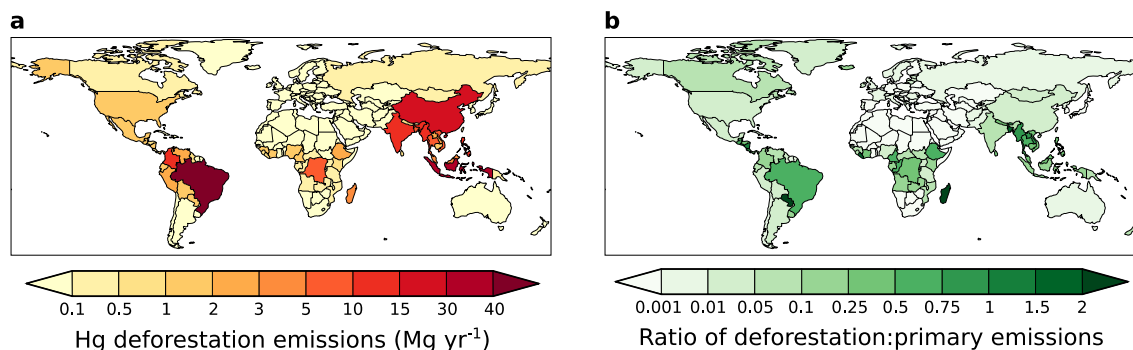
320 **Figure 1.** Comparison between modeled and observation-derived net emission factors (EFs) for
 321 deforestation in different regions. The upper panel shows total EFs and the lower panel shows the
 322 soil Hg^0 emissions component of deforestation EFs. Modeled circles show the best estimate
 323 (online simulations), while error bars show the 95% confidence interval due to model parameter
 324 uncertainties (calculated in offline simulations, Section S4). Observation estimates are from
 325 refs.^{18,21,24,46–62}, with the Amazon Total EF estimate based on measurements in Fig. S3. Observed
 326 error bars refer to uncertainty ranges when multiple plots were measured within a study (further
 327 information about these calculations can be found in Section S2 and the SI Spreadsheet).

328

329 We multiply the regional EFs by the deforested area from the CMIP6 Land-Use
 330 Harmonization (LUH2) dataset⁴⁵ to calculate the net Hg fluxes to the atmosphere from
 331 deforestation. Given the uncertain timescale for recovery in Hg sink capacity after
 332 deforestation, we assume that a deforested area has constant annual emissions over a
 333 considered time horizon. Previous LULCC studies for carbon suggest that forests recover
 334 their original biomass within 75 years after deforestation⁶³, so we employed time
 335 horizons between 15–60 years (Fig. S6) to calculate 2015 deforestation-driven emissions.

336 In Fig. 2a, we present country-level deforestation emissions based on a 45-year time
 337 horizon (emissions released from areas deforested between 1970 and 2014). Net
 338 emissions occurring in 2015 considering this 45-year deforestation time horizon are 217
 339 Mg yr^{-1} globally (CI: 134–1650 Mg yr^{-1}). Countries with substantial ($>10 \text{ Mg yr}^{-1}$)
 340 deforestation-driven emissions include Brazil (43 Mg yr^{-1}), Indonesia (35 Mg yr^{-1}), China
 341 (16 Mg yr^{-1}), Colombia (14 Mg yr^{-1}), India (13 Mg yr^{-1}), Philippines (11 Mg yr^{-1}), and
 342 Myanmar (11 Mg yr^{-1}). To put these emissions into context, Fig. 2b compares the
 343 deforestation emissions with 2015 primary anthropogenic emissions inventory from
 344 AMAP/UNEP^{9,38}. Deforestation Hg emissions are minor ($<5\%$) compared to primary
 345 anthropogenic emissions for most countries. However, for 32 countries, all located in the
 346 tropics, deforestation emissions are greater than 30% of primary emissions. For Brazil,
 347 which is the fifth highest emitter of primary Hg^{9,38}, deforestation emissions (43 Mg yr^{-1})
 348 are only 40% smaller than the 2015 emissions from primary anthropogenic sources (71
 349 Mg yr^{-1}). Deforestation emissions even exceed primary emissions in some countries,
 350 including Madagascar (deforestation emissions are 2.4 \times larger), Paraguay (2.3 \times), Liberia
 351 (2.0 \times), and Bangladesh (1.8 \times). Currently, Hg emissions inventories⁹ only consider
 352 primary anthropogenic emissions (2222 Mg yr^{-1} in 2015), overlooking deforestation as a
 353 significant source of anthropogenic Hg to the atmosphere (217 Mg yr^{-1}). The relative
 354 importance of deforestation as an anthropogenic driver of Hg pollution could increase
 355 over the next decades, with primary anthropogenic emissions of Hg projected to halve to
 356 1020 Mg yr^{-1} by 2035 under Minamata policies and reductions in fossil fuel use⁷⁰.
 357 Therefore, assessing the potential impacts of land use policy scenarios will be crucial for
 358 predicting future Hg cycling, as primary anthropogenic emissions decline in the future.

359



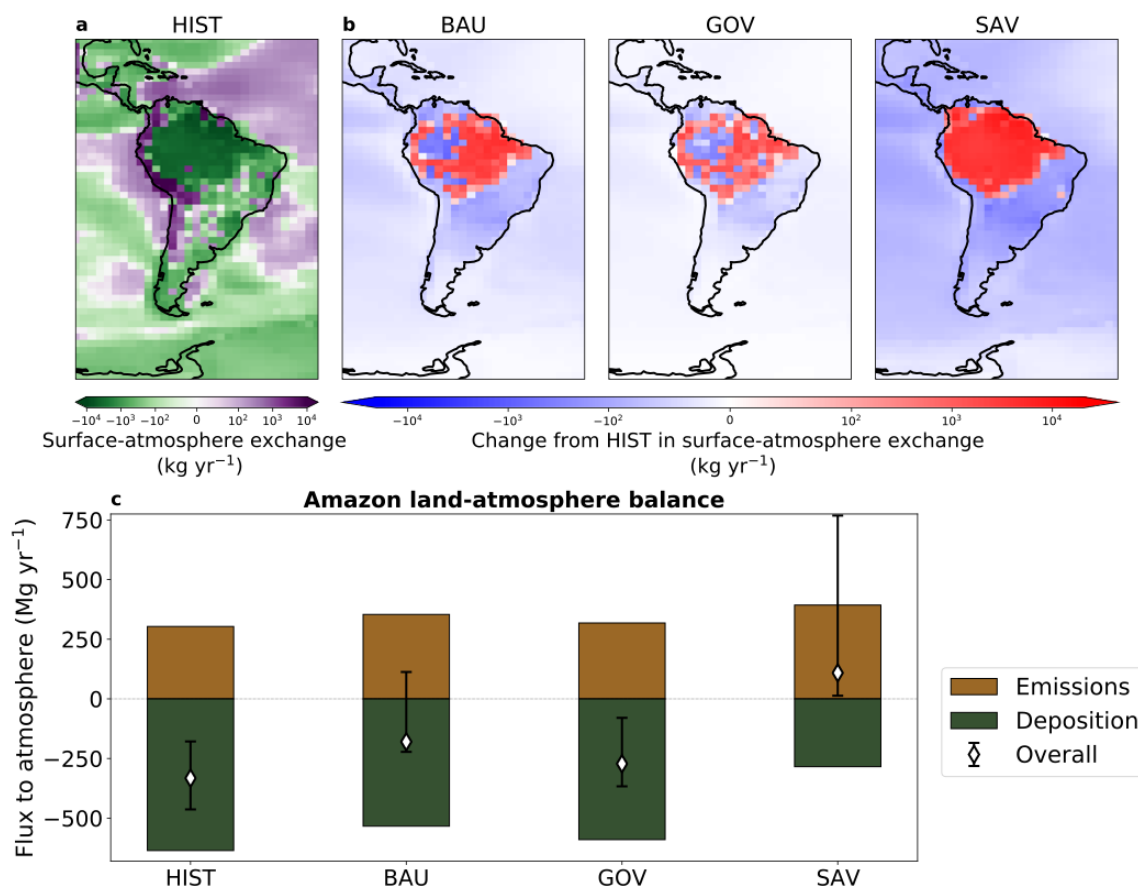
361 **Figure 2.** Country-level annual deforestation emissions of Hg in 2015. (a) Deforestation-driven
 362 net emissions of Hg by country, assuming that deforested areas from the previous 45 years
 363 (1970–2014) contribute to emissions. (b) Ratio of deforestation emissions to primary
 364 anthropogenic emissions^{9,38} by country.

365

366 **Amazon conservation policy impacts on Hg cycling.** The Amazon is one of the regions
 367 with the highest Hg fluxes from deforestation (Fig. 2) and land policy choices will
 368 determine how this evolves in the future. Under historical forest coverage from 2003
 369 (HIST simulation), the Amazon rainforest stands out as a strong global sink of Hg (Fig.
 370 3a), with net input from the atmosphere to the rainforest totaling 332 Mg yr⁻¹ (CI: 179–
 371 463 Mg yr⁻¹). We study the evolution of the Amazon Hg sink in two deforestation
 372 scenarios²⁷ for 2050: a business-as-usual scenario (BAU), which extrapolates historical
 373 deforestation tendencies into the future, and a governance scenario (GOV), which
 374 assumes expanded conservation of the rainforest in the future. In the BAU scenario,
 375 widespread deforestation, mainly in eastern Amazonia, reduces the net Hg inputs to soils
 376 (Fig. 3b). While the Amazon region overall remains a net Hg sink in BAU, the removed
 377 vegetation leads to decreased Hg⁰ deposition in the Amazon (change from HIST: -105
 378 Mg yr⁻¹; CI: -53 to -152 Mg yr⁻¹) and enhanced Hg⁰ emissions from soils (+35 Mg yr⁻¹ ;
 379 CI: 28–275 Mg yr⁻¹). For the Amazon policy scenarios, we have also considered the
 380 impact that fire-mediated forest clearing^{64,71} has on biomass burning emissions of Hg,
 381 which are 15 Mg yr⁻¹ (CI: 10–17 Mg yr⁻¹) larger in BAU than HIST. The BAU scenario
 382 shows atmospheric Hg⁰ concentrations increasing up to 0.3 ng m⁻³ (+50%) within the
 383 Amazon region (Fig. S11); this would be a detectable change in Hg⁰, comparable to the
 384 0.5 ng m⁻³ (-30%) decrease between 1995–2015 in North American Hg⁰ observations⁷².
 385 In the GOV scenario, deforestation is slowed by the conservation measures, leading to
 386 smaller perturbations in the dry deposition flux from HIST (-47 Mg yr⁻¹ ; CI: -25 to -68
 387 Mg yr⁻¹) and the soil emission flux (+16 Mg yr⁻¹; CI: 12–126 Mg yr⁻¹) (Fig. 3b). In GOV,
 388 burning emissions from deforestation are 1 Mg yr⁻¹ lower than in HIST, due to lower
 389 annual rates of deforestation in the 2050 GOV scenario compared to the HIST case
 390 representing 2003. Globally, the weakened rainforest sink of Hg yields higher deposition
 391 of Hg to oceans compared to the reference simulation (BAU – HIST = +108 Mg yr⁻¹;
 392 GOV – HIST = +44 Mg yr⁻¹).

393 Deforestation can be exacerbated through climate feedbacks, which are not considered in
394 these policy scenarios. For example, BAU projects that 40% of the Amazon will be
395 deforested by 2050²⁷, which could trigger a tipping point with widespread transition of
396 the rainforest to a savannah biome under diminished regional moisture recycling⁶⁶. To
397 evaluate this, we also re-ran an upper limit scenario from our previous work²³ where the
398 entire rainforest is converted to savannah (SAV). In this case, a strong decline in Hg⁰ dry
399 deposition (-359 Mg yr⁻¹; CI: -210 to -503 Mg yr⁻¹) and an increase in Hg⁰ soil emissions
400 (+89 Mg yr⁻¹; CI: 68 to 652 Mg yr⁻¹) drive enhanced inputs of Hg to the ocean (343 Mg
401 yr⁻¹) (Fig. 3b).

402 This change in the fate of atmospheric Hg (deposition to ocean instead of land) affects
403 both the spatial distribution and bioavailability of Hg pollution. When sequestered in
404 soils, Hg has an estimated residence time on the order of hundreds of years, whereas in
405 the surface ocean Hg is recycled to the atmosphere within months to years^{7,11}.
406 Deforestation thus increases the mobility of Hg by transferring Hg from locally-
407 sequestered reservoirs to the global pool. Human health risks are driven by exposure to
408 the more toxic form of the element, MeHg, which is produced through methylation in the
409 environment^{2,73}. Deforestation shifts Hg inputs from land to the ocean, where Hg can
410 more readily be methylated and bioaccumulate to dangerous levels in commercial fish.
411 Methylation and bioaccumulation of Hg can also occur in forested soils, but MeHg levels
412 in aquatic ecosystems are generally much higher (overall global ocean average = 15%)⁷⁴
413 than in Amazonian soils (1–5%)^{46,75}. In addition, the long length of aquatic food chains
414 leads to high levels of MeHg in commonly consumed fish species at higher trophic levels
415 (e.g., tuna, cod, and swordfish)⁷³.



416

417 **Figure 3.** Impacts of Amazon deforestation scenarios on surface-atmosphere Hg exchange. (a)
 418 The simulated surface-atmosphere exchange (net deposition is negative and net emission is
 419 positive) of Hg in the reference simulation (HIST). (b) Changes in exchange fluxes from HIST
 420 are shown for the deforestation scenarios: Business-as-usual (BAU), Governance (GOV), and
 421 Savannization (SAV); negative values refer to increased net fluxes to the surface compared to
 422 HIST and positive values refer to increased net fluxes to the atmosphere. (c) Total simulated
 423 fluxes of Hg emissions and deposition are calculated for the Amazon region in each scenario.
 424 White diamonds illustrate the net flux of Hg to the atmosphere (= emissions – deposition) and
 425 error bars refer to the 95% confidence interval based on model parameter uncertainties.

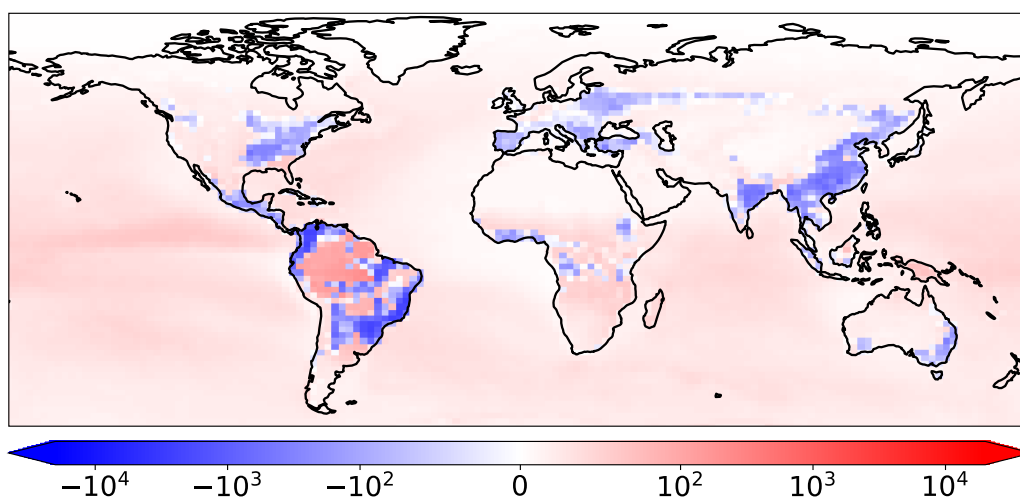
426

427 Deforestation policy substantially impacts the soil mass balance of Hg in the Amazon
 428 region, illustrated by our modeling simulations (Fig. 3c) and available field observations
 429 (Fig. S3). If agricultural expansion continues as in BAU, the Amazon sink of atmospheric
 430 Hg is weakened by 153 Mg yr⁻¹ (CI: 97–418 Mg yr⁻¹) (Fig. 3c). Under the more moderate
 431 GOV scenario, the Amazon Hg sink (272 Mg yr⁻¹; CI: 79–367 Mg yr⁻¹) is better
 432 preserved, though still 18% (CI: 14–65%) smaller than HIST. Stricter conservation
 433 policies in GOV yield an additional 92 Mg yr⁻¹ (CI: 59–234 Mg yr⁻¹) of Hg sequestered in

434 the Amazon compared to BAU. The SAV scenario illustrates that additional climate
435 feedbacks could flip the Amazon from a net Hg sink to a source (+109 Mg yr⁻¹; CI: 13–
436 768 Mg yr⁻¹). These Hg projections parallel recent findings on Amazon carbon cycling,
437 which have demonstrated that climate change and deforestation are turning the Amazon
438 into a CO₂ source²⁵. In addition to atmosphere-terrestrial exchange fluxes, soil erosion of
439 Hg can also be altered due to deforestation. We applied a soil erosion model GloSEM^{76,77}
440 to evaluate the impact of deforestation on erosion in the Amazon basin (Supplementary
441 Information Section S6). In terms of Hg flux magnitudes, perturbations to erosion are
442 smaller (<15%) than changes to the atmosphere-terrestrial exchange fluxes (Section S6),
443 which is supported by field studies⁶². Nevertheless, deforestation also enhances Hg
444 erosion in both scenarios (BAU: +33%; GOV: +14%), accelerating the transfer of
445 terrestrial Hg to aquatic ecosystems.

446 ***Quantifying the Hg mitigation potential of reforestation.*** Reforestation has been
447 identified as a potential mitigation approach for climate change, by strengthening the
448 terrestrial CO₂ sink^{30,78}. To investigate the concurrent strengthening of the terrestrial Hg
449 sink and the impacts on Hg cycling, we considered a global reforestation scenario (RFR)
450 based on the Global Reforestation Potential Map^{30,68}, which identified areas suitable for
451 reforestation worldwide (i.e., not including croplands or areas where forests are not
452 native). Figure 4 maps the impacts of reforestation on Hg surface-atmosphere exchange,
453 comparing to the reference HIST simulation. Net deposition of Hg increases over
454 reforested areas, declining over the ocean as well as land areas with existing forests.
455 Globally, RFR enhances uptake of Hg on land by 98 Mg yr⁻¹ (CI: 64–449 Mg yr⁻¹)
456 compared to HIST, thereby reducing Hg deposition to oceans. Reforestation could thus
457 take up approximately 5% of the anthropogenic Hg emission flux (~2200 Mg yr⁻¹)⁹. In
458 addition to the targeted benefits for biodiversity and climate change mitigation³⁰,
459 reforestation could moderately reduce levels of Hg in marine ecosystems, and thus
460 commercial fish. Nevertheless, the magnitude of reforestation impact (5% of primary

461 emissions) illustrates that reforestation is not a substitute for implementing extensive cuts
 462 to primary Hg emissions, like in the CO₂ context²⁹.



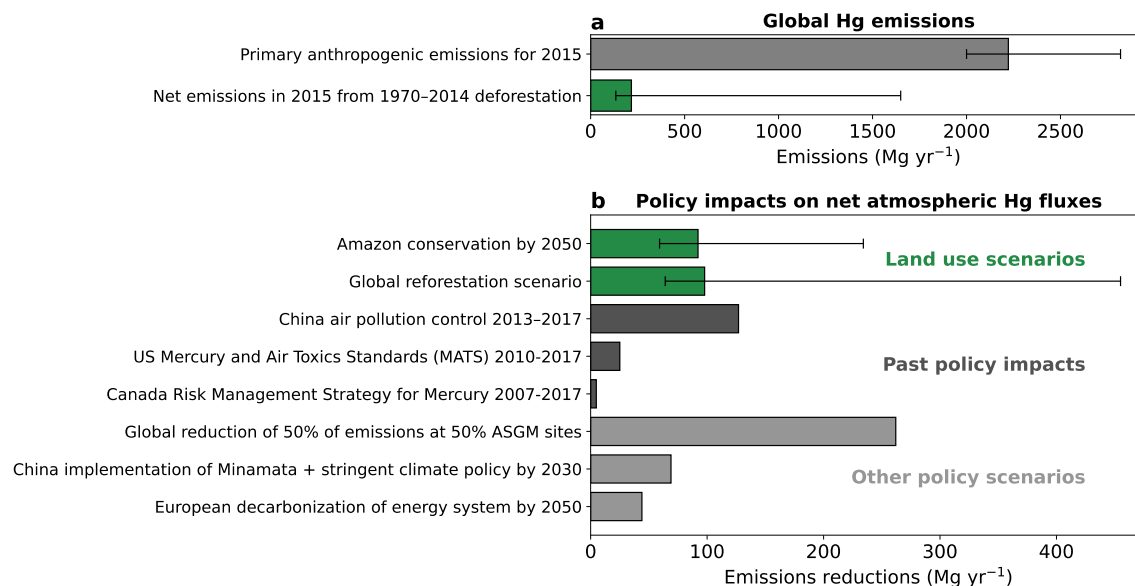
463 Reforestation change in surface-atmosphere exchange (kg yr⁻¹)

464 **Figure 4.** Enhanced land sink of Hg with reforestation. The impact of the potential reforestation
 465 (RFR) scenario on surface-atmosphere exchange. The differences from the reference (HIST)
 466 simulation are shown, with negative values referring to increased net fluxes to the surface and
 467 positive values referring to increased net fluxes to the atmosphere.
 468

469 Potential reforestation opportunities for Hg are dominated by the Amazon and Atlantic
 470 forest regions in South America (71 Mg yr⁻¹, 72% of total land sink impact) (Fig. 4). The
 471 potential reforestation impact on atmospheric fluxes in Northern extratropical areas alone
 472 (-29 Mg yr⁻¹) cannot compensate for increased deforestation Hg emissions in the Amazon
 473 (BAU: +153 Mg yr⁻¹; GOV: +61 Mg yr⁻¹). Overall, more information would be needed to
 474 compare the potentials of reforestation and conservation policies on a global scale, as the
 475 deforestation policy scenarios focused only on a specific region (the Amazon); future
 476 research could study conservation impacts in other tropical regions with high Hg
 477 deforestation emissions (Fig. 2) (e.g., in Africa and Southeast Asia). Our simulated fluxes
 478 consider the uptake of Hg upon maturation of forest stands, as reforested areas are
 479 assumed to have LAI of existent corresponding biomes. Further experimental research

480 would be required to understand the transient response of Hg uptake during the growth of
481 forests.

482 ***Implications for global Hg policy and caveats.*** Land use policy has been largely
483 unexplored as a lever to mitigate Hg pollution. On the global scale, the estimated
484 deforestation-driven Hg emissions in 2015 (217 Mg yr⁻¹; CI: 134–1650 Mg yr⁻¹)
485 correspond to 10% of the global primary anthropogenic emissions⁹ (2222 Mg yr⁻¹) (Fig.
486 5a). Therefore, though cutting primary anthropogenic emissions remains a priority,
487 deforestation fluxes should not be overlooked in assessments of Hg pollution, especially
488 for countries in the tropics (Fig. 2b). The potential of Amazon conservation and global
489 reforestation to reduce net Hg emissions in the future is substantial compared to
490 previously quantified policies aimed at tackling primary anthropogenic emissions (Fig.
491 5b). Potential emissions reductions from Amazon conservation (92 Mg yr⁻¹) and global
492 reforestation (98 Mg yr⁻¹) are within the range of impacts of past policy and future policy
493 scenarios aimed at reducing Hg from specific anthropogenic sources or due to national
494 climate and air pollution policies (5–262 Mg yr⁻¹)^{79–84}. Emissions reductions from land
495 use policies are different from primary emissions reductions in that their efficacy depends
496 on whether the storage of Hg in soils is over a long-term period. Similar to CO₂, the
497 potential benefits of enhanced Hg uptake on land can be reversed by human or natural
498 disturbances, e.g., by climate change increasing the frequency of wildfires — which re-
499 emit Hg and carbon from terrestrial ecosystems — and droughts — which reduce Hg and
500 CO₂ uptake by plants^{30,85}. Thus, mitigation of Hg pollution by conserving and increasing
501 forest area can only be realized with concurrent efforts to sustainably manage land areas
502 and preventing severe climate change. The potential of sustainable land use to mitigate
503 Hg pollution could enable collaborations between the Minamata Convention and other
504 global policy efforts to reduce deforestation, e.g., the 2021 Glasgow Declaration⁸⁶.



505

506

507

508

509

510

511

512

513

514

515

Figure 5. Potential of land use policies to reduce net Hg fluxes to the atmosphere. (a) Comparing global 2015 emissions from primary anthropogenic emissions^{9,38} and deforestation-driven emissions, assuming a 45-year time horizon (1970–2014 deforested areas). (b) Net Hg emissions reductions from land use policies (this study) are compared to primary anthropogenic emissions policies, whose impacts have been quantified in the literature^{79–84}. ASGM refers to artisanal and small-scale gold mining. For land use scenarios, “Amazon conservation by 2050” refers to the net emissions reductions in the 2050 governance (GOV) from the business-as-usual (BAU) simulations and “Global reforestation scenario” compares the net emissions reductions in the reforestation scenario (RFR) compared to the reference simulation (HIST). Error bars for this study refer to the 95% confidence interval based on model parameter uncertainties.

516

517

518

519

520

521

522

523

524

525

526

527

528

The current work provides an initial assessment of the global emissions of Hg from deforestation, which can spur future investigation into the impact of LULCC on Hg. Other LULCC processes (e.g., wood harvest and agricultural practices) may also affect Hg fluxes but have not been considered within this study. As well, due to the early stage of Hg research, we do not yet have the same level of information for Hg that is commonly included in LULCC assessments for carbon, including temporal information on the release of Hg from soils and Hg uptake rates during regrowth of vegetation²². Although we have assembled a dataset of available deforestation flux measurements covering multiple regions (SI Spreadsheet), there continues to be a lack of measurements in relevant regions (e.g., Afrotropic and Indomalayan) to constrain the response of Hg fluxes to deforestation, contributing uncertainty to this work. Further development of terrestrial Hg cycles and LULCC processes within Earth system models⁸⁷ will be vital to

529 investigate the evolution of the Hg land sink over time and the effect on environmental
530 Hg risks. Ultimately, mitigation of global Hg pollution depends not only on reducing
531 primary anthropogenic emissions, but also reducing anthropogenic activities like
532 deforestation that re-mobilize legacy Hg.

533

534 **Acknowledgments**

535 This work was funded by the Swiss National Science Foundation through an Early
536 Postdoc.Mobility grant to A.F. (P2EZP2_195424) and an Ambizione grant to M.J.
537 (PZ00P2_174101), a grant (#1924148) from the US National Science Foundation to
538 N.E.S., and an Academic Transition Grant from Eawag to J.B. We thank Ronny Meier
539 and Michael Windisch for assistance in processing the reforestation potential dataset. We
540 thank Luiz D. Lacerda for sharing Hg data from Brazil. We acknowledge all researchers
541 involved in conducting field studies measuring the impact of deforestation on Hg fluxes.

542

543 **Code and Data Availability**

544 Model code, analysis scripts, and simulation data supporting the results of this study are
545 published in Zenodo (<https://doi.org/10.5281/zenodo.8364698>) under a CC BY 4.0
546 license (<https://creativecommons.org/licenses/by/4.0/>).

547

548 **Associated Content**

549 *Supporting Information.* Further supporting information can be found in the following
550 files:

551 Soil emissions parametrization; Observations of deforestation fluxes; Global
552 deforestation-driven emissions estimates; Parameters for uncertainty analysis;
553 Scenario maps; Erosion calculations; Atmospheric concentration impacts (PDF)

554

555 Tabulated dataset of literature Hg deforestation flux measurements (XLSX)

556

557

558

559 **Author Contributions**

560 All authors conceived the study. M.J., J.B., and A.F. compiled Hg field data through
 561 literature review. A.F. and P.B performed the simulations. All authors contributed to the
 562 data analysis. A.F. wrote the draft of the paper with contributions and revisions from all
 563 authors.

564

565 **References**

- 566 (1) Sheehan, M. C.; Burke, T. A.; Navas-Acien, A.; Breyse, P. N.; McGready, J.; Fox, M. A.
 567 Global Methylmercury Exposure from Seafood Consumption and Risk of Developmental
 568 Neurotoxicity: A Systematic Review. *Bull. World Health Organ.* **2014**, 92 (4), 254-269F.
 569 <https://doi.org/10.2471/BLT.12.116152>.
- 570 (2) Zhang, Y.; Song, Z.; Huang, S.; Zhang, P.; Peng, Y.; Wu, P.; Gu, J.; Dutkiewicz, S.; Zhang,
 571 H.; Wu, S.; Wang, F.; Chen, L.; Wang, S.; Li, P. Global Health Effects of Future
 572 Atmospheric Mercury Emissions. *Nat Commun* **2021**, 12 (1), 3035.
 573 <https://doi.org/10.1038/s41467-021-23391-7>.
- 574 (3) Bellanger, M.; Pichery, C.; Aerts, D.; Berglund, M.; Castaño, A.; Čejchanová, M.; Crettaz,
 575 P.; Davidson, F.; Esteban, M.; Fischer, M. E.; Gurzau, A. E.; Halzlova, K.; Katsonouri, A.;
 576 Knudsen, L. E.; Kolossa-Gehring, M.; Koppen, G.; Ligocka, D.; Miklavčič, A.; Reis, M. F.;
 577 Rudnai, P.; Tratnik, J. S.; Weihe, P.; Budtz-Jørgensen, E.; Grandjean, P.; DEMO/COPHES.
 578 Economic Benefits of Methylmercury Exposure Control in Europe: Monetary Value of
 579 Neurotoxicity Prevention. *Environ Health* **2013**, 12 (1), 3. [https://doi.org/10.1186/1476-](https://doi.org/10.1186/1476-069X-12-3)
 580 [069X-12-3](https://doi.org/10.1186/1476-069X-12-3).
- 581 (4) Outridge, P. M.; Mason, R. P.; Wang, F.; Guerrero, S.; Heimbürger-Boavida, L. E. Updated
 582 Global and Oceanic Mercury Budgets for the United Nations Global Mercury Assessment
 583 2018. *Environ. Sci. Technol.* **2018**, [acs.est.8b01246](https://doi.org/10.1021/acs.est.8b01246).
 584 <https://doi.org/10.1021/acs.est.8b01246>.
- 585 (5) Shah, V.; Jacob, D. J.; Thackray, C. P.; Wang, X.; Sunderland, E. M.; Dibble, T. S.; Saiz-
 586 Lopez, A.; Černušák, I.; Kellö, V.; Castro, P. J.; Wu, R.; Wang, C. Improved Mechanistic
 587 Model of the Atmospheric Redox Chemistry of Mercury. *Environ. Sci. Technol.* **2021**, 55
 588 (21), 14445–14456. <https://doi.org/10.1021/acs.est.1c03160>.
- 589 (6) UNTC. *Minamata Convention on Mercury*; 2013.
 590 [https://treaties.un.org/Pages/ViewDetails.aspx?src=TREATY&mtdsg_no=XXVII-](https://treaties.un.org/Pages/ViewDetails.aspx?src=TREATY&mtdsg_no=XXVII-17&chapter=27)
 591 [17&chapter=27](https://treaties.un.org/Pages/ViewDetails.aspx?src=TREATY&mtdsg_no=XXVII-17&chapter=27).
- 592 (7) Amos, H. M.; Jacob, D. J.; Streets, D. G.; Sunderland, E. M. Legacy Impacts of All-Time
 593 Anthropogenic Emissions on the Global Mercury Cycle. *Global Biogeochem. Cycles* **2013**,
 594 27 (2), 410–421. <https://doi.org/10.1002/gbc.20040>.
- 595 (8) Zhou, J.; Obrist, D.; Dastoor, A.; Jiskra, M.; Ryjkov, A. Vegetation Uptake of Mercury and
 596 Impacts on Global Cycling. *Nat. Rev. Earth Environ.* **2021**, 2 (4), 269–284.
 597 <https://doi.org/10.1038/s43017-021-00146-y>.
- 598 (9) UNEP. *Global Mercury Assessment 2018*; UN Environment Programme, Chemicals and
 599 Health Branch. Geneva, Switzerland, 2019.
- 600 (10) Schaefer, K.; Elshorbany, Y.; Jafarov, E.; Schuster, P. F.; Striegl, R. G.; Wickland, K. P.;
 601 Sunderland, E. M. Potential Impacts of Mercury Released from Thawing Permafrost. *Nat*
 602 *Commun* **2020**, 11 (1), 4650. <https://doi.org/10.1038/s41467-020-18398-5>.

- 603 (11) Smith-Downey, N. V.; Sunderland, E. M.; Jacob, D. J. Anthropogenic Impacts on Global
604 Storage and Emissions of Mercury from Terrestrial Soils: Insights from a New Global
605 Model. *J. Geophys. Res.* **2010**, *115* (G3), G03008. <https://doi.org/10.1029/2009JG001124>.
- 606 (12) Jiskra, M.; Sonke, J. E.; Obrist, D.; Bieser, J.; Ebinghaus, R.; Myhre, C. L.; Pfaffhuber, K.
607 A.; Wängberg, I.; Kyllönen, K.; Worthy, D.; Martin, L. G.; Labuschagne, C.; Mkololo, T.;
608 Ramonet, M.; Magand, O.; Dommergue, A. A Vegetation Control on Seasonal Variations in
609 Global Atmospheric Mercury Concentrations. *Nature Geosci* **2018**, *11* (4), 244–250.
610 <https://doi.org/10.1038/s41561-018-0078-8>.
- 611 (13) Fostier, A. H.; Melendez-Perez, J. J.; Richter, L. Litter Mercury Deposition in the
612 Amazonian Rainforest. *Environ. Pollut.* **2015**, *206*, 605–610.
613 <https://doi.org/10.1016/j.envpol.2015.08.010>.
- 614 (14) IPCC. *Climate Change and Land: An IPCC Special Report on Climate Change,*
615 *Desertification, Land Degradation, Sustainable Land Management, Food Security, and*
616 *Greenhouse Gas Fluxes in Terrestrial Ecosystems*; Shukla, P. R., Skeg, J., Calvo Buendia,
617 E., Masson-Delmotte, V., Pörtner, H.-O., Roberts, D. C., Zhai, P., Slade, R., Connors, S.,
618 van Diemen, S., Ferrat, M., Haughey, E., Luz, S., Pathak, M., Petzold, J., Portugal Pereira,
619 J., Vyas, P., Huntley, E., Kissick, K., Belkacemi, M., Malley, J., Eds.; 2019.
- 620 (15) Zhang, H.; Holmes, C. D.; Wu, S. Impacts of Changes in Climate, Land Use and Land
621 Cover on Atmospheric Mercury. *Atmos. Environ.* **2016**, *141*, 230–244.
622 <https://doi.org/10.1016/j.atmosenv.2016.06.056>.
- 623 (16) UNFCCC. *The Paris Agreement*; 2015. [https://unfccc.int/process-and-meetings/the-paris-](https://unfccc.int/process-and-meetings/the-paris-agreement/the-paris-agreement)
624 [agreement/the-paris-agreement](https://unfccc.int/process-and-meetings/the-paris-agreement/the-paris-agreement).
- 625 (17) Adler Miserendino, R.; Guimarães, J. R. D.; Schudel, G.; Ghosh, S.; Godoy, J. M.;
626 Silbergeld, E. K.; Lees, P. S. J.; Bergquist, B. A. Mercury Pollution in Amapá, Brazil:
627 Mercury Amalgamation in Artisanal and Small-Scale Gold Mining or Land-Cover and
628 Land-Use Changes? *ACS Earth Space Chem.* **2018**, *2* (5), 441–450.
629 <https://doi.org/10.1021/acsearthspacechem.7b00089>.
- 630 (18) Carpi, A.; Fostier, A. H.; Orta, O. R.; dos Santos, J. C.; Gittings, M. Gaseous Mercury
631 Emissions from Soil Following Forest Loss and Land Use Changes: Field Experiments in
632 the United States and Brazil. *Atmos. Environ.* **2014**, *96*, 423–429.
633 <https://doi.org/10.1016/j.atmosenv.2014.08.004>.
- 634 (19) Melendez-Perez, J. J.; Fostier, A. H.; Carvalho, J. A.; Windmüller, C. C.; Santos, J. C.;
635 Carpi, A. Soil and Biomass Mercury Emissions during a Prescribed Fire in the Amazonian
636 Rain Forest. *Atmospheric Environment* **2014**, *96*, 415–422.
637 <https://doi.org/10.1016/j.atmosenv.2014.06.032>.
- 638 (20) Roulet, M.; Lucotte, M.; Farella, N.; Serique, G.; Coelho, H.; Passos, S.; Mergler, D.
639 Effects of Recent Human Colonization on the Presence of Mercury in Amazonian
640 Ecosystems. *Water Air Soil Pollut.* **1999**, *112*, 297–313.
- 641 (21) Fostier, A. H.; Forti, M. C.; Guimarães, J. R.; Melfi, A. J.; Boulet, R.; Espirito Santo, C. M.;
642 Krug, F. J. Mercury Fluxes in a Natural Forested Amazonian Catchment (Serra Do Navio,
643 Amapá State, Brazil). *Sci. Total Environ.* **2000**, *260* (1–3), 201–211.
644 [https://doi.org/10.1016/S0048-9697\(00\)00564-7](https://doi.org/10.1016/S0048-9697(00)00564-7).
- 645 (22) Obermeier, W. A.; Nabel, J. E. M. S.; Loughran, T.; Hartung, K.; Bastos, A.; Havermann,
646 F.; Anthoni, P.; Arneith, A.; Goll, D. S.; Lienert, S.; Lombardozi, D.; Luyssaert, S.;
647 McGuire, P. C.; Melton, J. R.; Poulter, B.; Sitch, S.; Sullivan, M. O.; Tian, H.; Walker, A.
648 P.; Wiltshire, A. J.; Zaehle, S.; Pongratz, J. Modelled Land Use and Land Cover Change
649 Emissions – a Spatio-Temporal Comparison of Different Approaches. *Earth Syst. Dynam.*
650 **2021**, *12* (2), 635–670. <https://doi.org/10.5194/esd-12-635-2021>.

- 651 (23) Feinberg, A.; Dlamini, T.; Jiskra, M.; Shah, V.; Selin, N. E. Evaluating Atmospheric
652 Mercury (Hg) Uptake by Vegetation in a Chemistry-Transport Model. *Environ. Sci.:*
653 *Processes Impacts* **2022**, *24* (9), 1303–1318. <https://doi.org/10.1039/D2EM00032F>.
- 654 (24) Wang, X.; Lin, C.-J.; Yuan, W.; Sommar, J.; Zhu, W.; Feng, X. Emission-Dominated Gas
655 Exchange of Elemental Mercury Vapor over Natural Surfaces in China. *Atmos. Chem. Phys.*
656 **2016**, *16* (17), 11125–11143. <https://doi.org/10.5194/acp-16-11125-2016>.
- 657 (25) Gatti, L. V.; Basso, L. S.; Miller, J. B.; Gloor, M.; Gatti Domingues, L.; Cassol, H. L. G.;
658 Tejada, G.; Aragão, L. E. O. C.; Nobre, C.; Peters, W.; Marani, L.; Arai, E.; Sanches, A. H.;
659 Corrêa, S. M.; Anderson, L.; Von Randow, C.; Correia, C. S. C.; Crispim, S. P.; Neves, R.
660 A. L. Amazonia as a Carbon Source Linked to Deforestation and Climate Change. *Nature*
661 **2021**, *595* (7867), 388–393. <https://doi.org/10.1038/s41586-021-03629-6>.
- 662 (26) Tyukavina, A.; Hansen, M. C.; Potapov, P. V.; Stehman, S. V.; Smith-Rodriguez, K.; Okpa,
663 C.; Aguilar, R. Types and Rates of Forest Disturbance in Brazilian Legal Amazon, 2000–
664 2013. *Sci. Adv.* **2017**, *3* (4), e1601047. <https://doi.org/10.1126/sciadv.1601047>.
- 665 (27) Soares-Filho, B. S.; Nepstad, D. C.; Curran, L. M.; Cerqueira, G. C.; Garcia, R. A.; Ramos,
666 C. A.; Voll, E.; McDonald, A.; Lefebvre, P.; Schlesinger, P. Modelling Conservation in the
667 Amazon Basin. *Nature* **2006**, *440* (7083), 520–523. <https://doi.org/10.1038/nature04389>.
- 668 (28) IPCC. Summary for Policymakers. In *Climate Change 2022: Mitigation of Climate Change. Contribution of Working Group III to the Sixth Assessment Report of the Intergovernmental Panel on Climate Change*; [P.R. Shukla, J. Skea, R. Slade, A. Al Khourdajie, R. van Diemen, D. McCollum, M. Pathak, S. Some, P. Vyas, R. Fradera, M. Belkacemi, A. Hasija, G. Lisboa, S. Luz, J. Malley, (eds.)]. Cambridge University Press, Cambridge, UK and New York, NY, USA.
- 674 (29) Holl, K. D.; Brancalion, P. H. S. Tree Planting Is Not a Simple Solution. *Science* **2020**, *368*
675 (6491), 580–581. <https://doi.org/10.1126/science.aba8232>.
- 676 (30) Griscom, B. W.; Adams, J.; Ellis, P. W.; Houghton, R. A.; Lomax, G.; Miteva, D. A.;
677 Schlesinger, W. H.; Shoch, D.; Siikamäki, J. V.; Smith, P.; Woodbury, P.; Zganjar, C.;
678 Blackman, A.; Campari, J.; Conant, R. T.; Delgado, C.; Elias, P.; Gopalakrishna, T.;
679 Hamsik, M. R.; Herrero, M.; Kiesecker, J.; Landis, E.; Laestadius, L.; Leavitt, S. M.;
680 Minnemeyer, S.; Polasky, S.; Potapov, P.; Putz, F. E.; Sanderman, J.; Silvius, M.;
681 Wollenberg, E.; Fargione, J. Natural Climate Solutions. *Proc. Natl. Acad. Sci. U.S.A.* **2017**,
682 *114* (44), 11645–11650. <https://doi.org/10.1073/pnas.1710465114>.
- 683 (31) Gelaro, R.; McCarty, W.; Suárez, M. J.; Todling, R.; Molod, A.; Takacs, L.; Randles, C. A.;
684 Darmenov, A.; Bosilovich, M. G.; Reichle, R.; Wargan, K.; Coy, L.; Cullather, R.; Draper,
685 C.; Akella, S.; Buchard, V.; Conaty, A.; Silva, A. M. da; Gu, W.; Kim, G.-K.; Koster, R.;
686 Lucchesi, R.; Merkova, D.; Nielsen, J. E.; Partyka, G.; Pawson, S.; Putman, W.; Rienecker,
687 M.; Schubert, S. D.; Sienkiewicz, M.; Zhao, B. The Modern-Era Retrospective Analysis for
688 Research and Applications, Version 2 (MERRA-2). *J. Clim.* **2017**, *30* (14), 5419–5454.
689 <https://doi.org/10.1175/JCLI-D-16-0758.1>.
- 690 (32) Horowitz, H. M.; Jacob, D. J.; Zhang, Y.; Dibble, T. S.; Slemr, F.; Amos, H. M.; Schmidt,
691 J. A.; Corbitt, E. S.; Marais, E. A.; Sunderland, E. M. A New Mechanism for Atmospheric
692 Mercury Redox Chemistry: Implications for the Global Mercury Budget. *Atmos. Chem.*
693 *Phys.* **2017**, *17* (10), 6353–6371. <https://doi.org/10.5194/acp-17-6353-2017>.
- 694 (33) Amos, H. M.; Jacob, D. J.; Holmes, C. D.; Fisher, J. A.; Wang, Q.; Yantosca, R. M.;
695 Corbitt, E. S.; Galarneau, E.; Rutter, A. P.; Gustin, M. S.; Steffen, A.; Schauer, J. J.;
696 Graydon, J. A.; Louis, V. L. St.; Talbot, R. W.; Edgerton, E. S.; Zhang, Y.; Sunderland, E.
697 M. Gas-Particle Partitioning of Atmospheric Hg(II) and Its Effect on Global Mercury
698 Deposition. *Atmos. Chem. Phys.* **2012**, *12* (1), 591–603. [https://doi.org/10.5194/acp-12-591-](https://doi.org/10.5194/acp-12-591-2012)
699 2012.

- 700 (34) Wang, Y.; Jacob, D. J.; Logan, J. A. Global Simulation of Tropospheric O₃-NO_x-
701 Hydrocarbon Chemistry: 1. Model Formulation. *J. Geophys. Res.* **1998**, *103* (D9), 10713–
702 10725. <https://doi.org/10.1029/98JD00158>.
- 703 (35) Fisher, J. A.; Jacob, D. J.; Wang, Q.; Bahreini, R.; Carouge, C. C.; Cubison, M. J.; Dibb, J.
704 E.; Diehl, T.; Jimenez, J. L.; Leibensperger, E. M.; Lu, Z.; Meinders, M. B. J.; Pye, H. O.
705 T.; Quinn, P. K.; Sharma, S.; Streets, D. G.; van Donkelaar, A.; Yantosca, R. M. Sources,
706 Distribution, and Acidity of Sulfate–Ammonium Aerosol in the Arctic in Winter–Spring.
707 *Atmos. Environ.* **2011**, *45* (39), 7301–7318. <https://doi.org/10.1016/j.atmosenv.2011.08.030>.
- 708 (36) Gibbs, H. K. Olson’s Major World Ecosystem Complexes Ranked by Carbon in Live
709 Vegetation: An Updated Database Using the GLC2000 Land Cover Product (NDP-017b).
710 <https://www.osti.gov/biblio/1389498>, 2006. **2006**.
- 711 (37) Yuan, H.; Dai, Y.; Xiao, Z.; Ji, D.; Shangguan, W. Reprocessing the MODIS Leaf Area
712 Index Products for Land Surface and Climate Modelling. *Remote Sens. Environ.* **2011**, *115*
713 (5), 1171–1187. <https://doi.org/10.1016/j.rse.2011.01.001>.
- 714 (38) Steenhuisen, F.; Wilson, S. J. Development and Application of an Updated Geospatial
715 Distribution Model for Gridding 2015 Global Mercury Emissions. *Atmos. Environ.* **2019**,
716 *211*, 138–150. <https://doi.org/10.1016/j.atmosenv.2019.05.003>.
- 717 (39) van der Werf, G. R.; Randerson, J. T.; Giglio, L.; van Leeuwen, T. T.; Chen, Y.; Rogers, B.
718 M.; Mu, M.; van Marle, M. J. E.; Morton, D. C.; Collatz, G. J.; Yokelson, R. J.; Kasibhatla,
719 P. S. Global Fire Emissions Estimates during 1997–2016. *Earth Syst. Sci. Data* **2017**, *9* (2),
720 697–720. <https://doi.org/10.5194/essd-9-697-2017>.
- 721 (40) Strode, S. A.; Jaeglé, L.; Selin, N. E.; Jacob, D. J.; Park, R. J.; Yantosca, R. M.; Mason, R.
722 P.; Slemr, F. Air-Sea Exchange in the Global Mercury Cycle. *Global Biogeochem. Cycles*
723 **2007**, *21* (1), GB1017. <https://doi.org/10.1029/2006GB002766>.
- 724 (41) Khan, T. R.; Obrist, D.; Agnan, Y.; Selin, N. E.; Perlinger, J. A. Atmosphere-Terrestrial
725 Exchange of Gaseous Elemental Mercury: Parameterization Improvement through Direct
726 Comparison with Measured Ecosystem Fluxes. *Environ. Sci.: Processes Impacts* **2019**, *21*
727 (10), 1699–1712. <https://doi.org/10.1039/C9EM00341J>.
- 728 (42) Selin, N. E.; Jacob, D. J.; Yantosca, R. M.; Strode, S.; Jaeglé, L.; Sunderland, E. M. Global
729 3-D Land-Ocean-Atmosphere Model for Mercury: Present-Day versus Preindustrial Cycles
730 and Anthropogenic Enrichment Factors for Deposition. *Global Biogeochem. Cycles* **2008**,
731 *22* (2), GB2011. <https://doi.org/10.1029/2007GB003040>.
- 732 (43) Verstraete, M. M. Radiation Transfer in Plant Canopies: Transmission of Direct Solar
733 Radiation and the Role of Leaf Orientation. *J. Geophys. Res.* **1987**, *92* (D9), 10985.
734 <https://doi.org/10.1029/JD092iD09p10985>.
- 735 (44) Dinerstein, E.; Olson, D.; Joshi, A.; Vynne, C.; Burgess, N. D.; Wikramanayake, E.; Hahn,
736 N.; Palminteri, S.; Hedao, P.; Noss, R.; Hansen, M.; Locke, H.; Ellis, E. C.; Jones, B.;
737 Barber, C. V.; Hayes, R.; Kormos, C.; Martin, V.; Crist, E.; Sechrest, W.; Price, L.; Baillie,
738 J. E. M.; Weeden, D.; Suckling, K.; Davis, C.; Sizer, N.; Moore, R.; Thau, D.; Birch, T.;
739 Potapov, P.; Turubanova, S.; Tyukavina, A.; de Souza, N.; Pintea, L.; Brito, J. C.;
740 Llewellyn, O. A.; Miller, A. G.; Patzelt, A.; Ghazanfar, S. A.; Timberlake, J.; Klöser, H.;
741 Shennan-Farpon, Y.; Kindt, R.; Lillesø, J.-P. B.; van Breugel, P.; Graudal, L.; Voge, M.;
742 Al-Shammari, K. F.; Saleem, M. An Ecoregion-Based Approach to Protecting Half the
743 Terrestrial Realm. *BioScience* **2017**, *67* (6), 534–545. <https://doi.org/10.1093/biosci/bix014>.
- 744 (45) Hurtt, G. C.; Chini, L.; Sahajpal, R.; Froliking, S.; Bodirsky, B. L.; Calvin, K.; Doelman, J.
745 C.; Fisk, J.; Fujimori, S.; Klein Goldewijk, K.; Hasegawa, T.; Havlik, P.; Heinemann, A.;
746 Humpenöder, F.; Jungclaus, J.; Kaplan, J. O.; Kennedy, J.; Krisztin, T.; Lawrence, D.;
747 Lawrence, P.; Ma, L.; Mertz, O.; Pongratz, J.; Popp, A.; Poulter, B.; Riahi, K.; Shevliakova,
748 E.; Stehfest, E.; Thornton, P.; Tubiello, F. N.; van Vuuren, D. P.; Zhang, X. Harmonization

- 749 of Global Land Use Change and Management for the Period 850–2100 (LUH2) for CMIP6.
 750 *Geosci. Model Dev.* **2020**, *13* (11), 5425–5464. <https://doi.org/10.5194/gmd-13-5425-2020>.
- 751 (46) Gerson, J. R.; Szponar, N.; Zambrano, A. A.; Bergquist, B.; Broadbent, E.; Driscoll, C. T.;
 752 Erkenswick, G.; Evers, D. C.; Fernandez, L. E.; Hsu-Kim, H.; Inga, G.; Lansdale, K. N.;
 753 Marchese, M. J.; Martinez, A.; Moore, C.; Pan, W. K.; Purizaca, R. P.; Sánchez, V.; Silman,
 754 M.; Ury, E. A.; Vega, C.; Watsa, M.; Bernhardt, E. S. Amazon Forests Capture High Levels
 755 of Atmospheric Mercury Pollution from Artisanal Gold Mining. *Nat Commun* **2022**, *13* (1),
 756 559. <https://doi.org/10.1038/s41467-022-27997-3>.
- 757 (47) Almeida, M. D.; Lacerda, L. D.; Bastos, W. R.; Herrmann, J. C. Mercury Loss from Soils
 758 Following Conversion from Forest to Pasture in Rondônia, Western Amazon, Brazil.
 759 *Environmental Pollution* **2005**, *137* (2), 179–186.
 760 <https://doi.org/10.1016/j.envpol.2005.02.026>.
- 761 (48) Almeida, M. D.; Marins, R. V.; Paraquetti, H. H. M.; Bastos, W. R.; Lacerda, L. D.
 762 Mercury Degassing from Forested and Open Field Soils in Rondônia, Western Amazon,
 763 Brazil. *Chemosphere* **2009**, *77* (1), 60–66.
 764 <https://doi.org/10.1016/j.chemosphere.2009.05.018>.
- 765 (49) Lacerda, L. D.; de Souza, M.; Ribeiro, M. G. The Effects of Land Use Change on Mercury
 766 Distribution in Soils of Alta Floresta, Southern Amazon. *Environmental Pollution* **2004**,
 767 *129* (2), 247–255. <https://doi.org/10.1016/j.envpol.2003.10.013>.
- 768 (50) Béliveau, A.; Lucotte, M.; Davidson, R.; do Canto Lopes, L. O.; Paquet, S. Early Hg
 769 Mobility in Cultivated Tropical Soils One Year after Slash-and-Burn of the Primary Forest,
 770 in the Brazilian Amazon. *Science of The Total Environment* **2009**, *407* (15), 4480–4489.
 771 <https://doi.org/10.1016/j.scitotenv.2009.04.012>.
- 772 (51) Béliveau, A.; Lucotte, M.; Davidson, R.; Paquet, S.; Mertens, F.; Passos, C. J.; Romana, C.
 773 A. Reduction of Soil Erosion and Mercury Losses in Agroforestry Systems Compared to
 774 Forests and Cultivated Fields in the Brazilian Amazon. *Journal of Environmental*
 775 *Management* **2017**, *203*, 522–532. <https://doi.org/10.1016/j.jenvman.2017.07.037>.
- 776 (52) Patry, C.; Davidson, R.; Lucotte, M.; Béliveau, A. Impact of Forested Fallows on Fertility
 777 and Mercury Content in Soils of the Tapajós River Region, Brazilian Amazon. *Science of*
 778 *The Total Environment* **2013**, *458–460*, 228–237.
 779 <https://doi.org/10.1016/j.scitotenv.2013.04.037>.
- 780 (53) Comte, I.; Lucotte, M.; Davidson, R.; Reis de Carvalho, C. J.; de Assis Oliveira, F.;
 781 Rousseau, G. X. Impacts of Land Uses on Mercury Retention in Long-Time Cultivated
 782 Soils, Brazilian Amazon. *Water Air Soil Pollut* **2013**, *224* (4), 1515.
 783 <https://doi.org/10.1007/s11270-013-1515-3>.
- 784 (54) Magarelli, G.; Fostier, A. Influence of Deforestation on the Mercury Air/Soil Exchange in
 785 the Negro River Basin, Amazon. *Atmos. Environ.* **2005**, *39* (39), 7518–7528.
 786 <https://doi.org/10.1016/j.atmosenv.2005.07.067>.
- 787 (55) Mainville, N.; Webb, J.; Lucotte, M.; Davidson, R.; Betancourt, O.; Cueva, E.; Mergler, D.
 788 Decrease of Soil Fertility and Release of Mercury Following Deforestation in the Andean
 789 Amazon, Napo River Valley, Ecuador. *Science of The Total Environment* **2006**, *368* (1),
 790 88–98. <https://doi.org/10.1016/j.scitotenv.2005.09.064>.
- 791 (56) Roulet, M.; Lucotte, M.; Saint-Aubin, A.; Tran, S.; Rhéault, I.; Farella, N.; De Jesus Da
 792 Silva, E.; Dezencourt, J.; Sousa Passos, C.-J.; Santos Soares, G.; Guimarães, J.-R. D.;
 793 Mergler, D.; Amorim, M. The Geochemistry of Mercury in Central Amazonian Soils
 794 Developed on the Alter-Do-Chão Formation of the Lower Tapajós River Valley, Pará State,
 795 Brazil. *Science of The Total Environment* **1998**, *223* (1), 1–24.
 796 [https://doi.org/10.1016/S0048-9697\(98\)00265-4](https://doi.org/10.1016/S0048-9697(98)00265-4).

- 797 (57) Wasserman, J. C.; Campos, R. C.; Hacon, S. de S.; Farias, R. A.; Caires, S. M. Mercury in
798 Soils and Sediments from Gold Mining Liabilities in Southern Amazonia. *Quím. Nova*
799 **2007**, *30* (4). <https://doi.org/10.1590/S0100-40422007000400003>.
- 800 (58) Homann, P. S.; Darbyshire, R. L.; Bormann, B. T.; Morrissette, B. A. Forest Structure
801 Affects Soil Mercury Losses in the Presence and Absence of Wildfire. *Environ. Sci.*
802 *Technol.* **2015**, *49* (21), 12714–12722. <https://doi.org/10.1021/acs.est.5b03355>.
- 803 (59) Gamby, R. L.; Hammerschmidt, C. R.; Costello, D. M.; Lamborg, C. H.; Runkle, J. R.
804 Deforestation and Cultivation Mobilize Mercury from Topsoil. *Science of The Total*
805 *Environment* **2015**, *532*, 467–473. <https://doi.org/10.1016/j.scitotenv.2015.06.025>.
- 806 (60) Mazur, M.; Mitchell, C. P. J.; Eckley, C. S.; Eggert, S. L.; Kolka, R. K.; Sebestyen, S. D.;
807 Swain, E. B. Gaseous Mercury Fluxes from Forest Soils in Response to Forest Harvesting
808 Intensity: A Field Manipulation Experiment. *Science of The Total Environment* **2014**, *496*,
809 678–687. <https://doi.org/10.1016/j.scitotenv.2014.06.058>.
- 810 (61) Ma, M.; Wang, D.; Sun, R.; Shen, Y.; Huang, L. Gaseous Mercury Emissions from
811 Subtropical Forested and Open Field Soils in a National Nature Reserve, Southwest China.
812 *Atmospheric Environment* **2013**, *64*, 116–123.
813 <https://doi.org/10.1016/j.atmosenv.2012.09.038>.
- 814 (62) Eckley, C. S.; Eagles-Smith, C.; Tate, M. T.; Krabbenhoft, D. P. Surface-Air Mercury
815 Fluxes and a Watershed Mass Balance in Forested and Harvested Catchments.
816 *Environmental Pollution* **2021**, *277*, 116869. <https://doi.org/10.1016/j.envpol.2021.116869>.
- 817 (63) Ramankutty, N.; Gibbs, H. K.; Achard, F.; Defries, R.; Foley, J. A.; Houghton, R. A.
818 Challenges to Estimating Carbon Emissions from Tropical Deforestation. *Global Change*
819 *Biol* **2007**, *13* (1), 51–66. <https://doi.org/10.1111/j.1365-2486.2006.01272.x>.
- 820 (64) Crespo-Lopez, M. E.; Augusto-Oliveira, M.; Lopes-Araújo, A.; Santos-Sacramento, L.;
821 Yuki Takeda, P.; Macchi, B. de M.; do Nascimento, J. L. M.; Maia, C. S. F.; Lima, R. R.;
822 Arrifano, G. P. Mercury: What Can We Learn from the Amazon? *Environment*
823 *International* **2021**, *146*, 106223. <https://doi.org/10.1016/j.envint.2020.106223>.
- 824 (65) Michelazzo, P. A. M.; Fostier, A. H.; Magarelli, G.; Santos, J. C.; de Carvalho, J. A.
825 Mercury Emissions from Forest Burning in Southern Amazon. *Geophys. Res. Lett.* **2010**, *37*
826 (9), L09809. <https://doi.org/10.1029/2009GL042220>.
- 827 (66) Lovejoy, T. E.; Nobre, C. Amazon Tipping Point. *Sci. Adv.* **2018**, *4* (2), eaat2340.
- 828 (67) Alves de Oliveira, B. F.; Bottino, M. J.; Nobre, P.; Nobre, C. A. Deforestation and Climate
829 Change Are Projected to Increase Heat Stress Risk in the Brazilian Amazon. *Commun.*
830 *Earth Environ.* **2021**, *2* (1), 207. <https://doi.org/10.1038/s43247-021-00275-8>.
- 831 (68) Griscom, B. W.; Adams, J.; Ellis, P. W.; Houghton, R. A.; Lomax, G.; Miteva, D. A.;
832 Schlesinger, W. H.; Shoch, D.; Siikamäki, J. V.; Smith, P.; Woodbury, P.; Zganjar, C.;
833 Blackman, A.; Campari, J.; Conant, R. T.; Delgado, C.; Elias, P.; Gopalakrishna, T.;
834 Hamsik, M. R.; Herrero, M.; Kiesecker, J.; Landis, E.; Laestadius, L.; Leavitt, S. M.;
835 Minnemeyer, S.; Polasky, S.; Potapov, P.; Putz, F. E.; Sanderman, J.; Silvius, M.;
836 Wollenberg, E.; Fargione, J. *Global Reforestation Potential Map*; Zenodo, 2017.
837 <https://doi.org/10.5281/zenodo.883444>.
- 838 (69) McKay, M. D.; Beckman, R. J.; Conover, W. J. Comparison of Three Methods for Selecting
839 Values of Input Variables in the Analysis of Output from a Computer Code. *Technometrics*
840 **1979**, *21* (2), 239–245. <https://doi.org/10.1080/00401706.1979.10489755>.
- 841 (70) Pacyna, J. M.; Travníkov, O.; De Simone, F.; Hedgecock, I. M.; Sundseth, K.; Pacyna, E.
842 G.; Steenhuisen, F.; Pirrone, N.; Munthe, J.; Kindbom, K. Current and Future Levels of
843 Mercury Atmospheric Pollution on a Global Scale. *Atmos. Chem. Phys.* **2016**, *16* (19),
844 12495–12511. <https://doi.org/10.5194/acp-16-12495-2016>.
- 845 (71) Fisher, J. A.; Schneider, L.; Fostier, A.-H.; Guerrero, S.; Guimarães, J. R. D.; Labuschagne,
846 C.; Leaner, J. J.; Martin, L. G.; Mason, R. P.; Somerset, V.; Walters, C. A Synthesis of

- 847 Mercury Research in the Southern Hemisphere, Part 2: Anthropogenic Perturbations. *Ambio*
848 **2023**, 52 (5), 918–937. <https://doi.org/10.1007/s13280-023-01840-5>.
- 849 (72) Zhang, Y.; Jacob, D. J.; Horowitz, H. M.; Chen, L.; Amos, H. M.; Krabbenhoft, D. P.;
850 Slemr, F.; St. Louis, V. L.; Sunderland, E. M. Observed Decrease in Atmospheric Mercury
851 Explained by Global Decline in Anthropogenic Emissions. *Proc. Natl. Acad. Sci. U.S.A.*
852 **2016**, 113 (3), 526–531. <https://doi.org/10.1073/pnas.1516312113>.
- 853 (73) Schartup, A. T.; Thackray, C. P.; Qureshi, A.; Dassuncao, C.; Gillespie, K.; Hanke, A.;
854 Sunderland, E. M. Climate Change and Overfishing Increase Neurotoxicant in Marine
855 Predators. *Nature* **2019**, 572 (7771), 648–650. <https://doi.org/10.1038/s41586-019-1468-9>.
- 856 (74) Zhang, Y.; Soerensen, A. L.; Schartup, A. T.; Sunderland, E. M. A Global Model for
857 Methylmercury Formation and Uptake at the Base of Marine Food Webs. *Global*
858 *Biogeochem. Cycles* **2020**, 34 (2). <https://doi.org/10.1029/2019GB006348>.
- 859 (75) Roulet, M.; Guimarães, J.R.D.; Lucotte, M. Methylmercury Production and Accumulation in
860 Sediments and Soils of an Amazonian Floodplain – Effect of Seasonal Inundation. *Water,*
861 *Air, and Soil Pollution* **2001**, 128, 41–60.
- 862 (76) Borrelli, P.; Robinson, D. A.; Panagos, P.; Lugato, E.; Yang, J. E.; Alewell, C.; Wuepper,
863 D.; Montanarella, L.; Ballabio, C. Land Use and Climate Change Impacts on Global Soil
864 Erosion by Water (2015–2070). *Proc. Natl. Acad. Sci. U.S.A.* **2020**, 117 (36), 21994–22001.
865 <https://doi.org/10.1073/pnas.2001403117>.
- 866 (77) Borrelli, P.; Robinson, D. A.; Fleischer, L. R.; Lugato, E.; Ballabio, C.; Alewell, C.;
867 Meusburger, K.; Modugno, S.; Schütt, B.; Ferro, V.; Bagarello, V.; Oost, K. V.;
868 Montanarella, L.; Panagos, P. An Assessment of the Global Impact of 21st Century Land
869 Use Change on Soil Erosion. *Nat Commun* **2017**, 8 (1), 2013.
870 <https://doi.org/10.1038/s41467-017-02142-7>.
- 871 (78) Bastin, J.-F.; Finegold, Y.; Garcia, C.; Mollicone, D.; Rezende, M.; Routh, D.; Zohner, C.
872 M.; Crowther, T. W. The Global Tree Restoration Potential. *Science* **2019**, 365 (6448), 76–
873 79. <https://doi.org/10.1126/science.aax0848>.
- 874 (79) Liu, K.; Wu, Q.; Wang, L.; Wang, S.; Liu, T.; Ding, D.; Tang, Y.; Li, G.; Tian, H.; Duan,
875 L.; Wang, X.; Fu, X.; Feng, X.; Hao, J. Measure-Specific Effectiveness of Air Pollution
876 Control on China’s Atmospheric Mercury Concentration and Deposition during 2013–2017.
877 *Environ. Sci. Technol.* **2019**, 53 (15), 8938–8946. <https://doi.org/10.1021/acs.est.9b02428>.
- 878 (80) EPA. *National Emission Standards for Hazardous Air Pollutants: Coal- and Oil-Fired*
879 *Electric Utility Steam Generating Units—Reconsideration of Supplemental Finding and*
880 *Residual Risk and Technology Review*; EPA–HQ–OAR–2018–0794; FRL–9988–93–OAR;
881 2019; pp 2670–2704. <https://www.govinfo.gov/content/pkg/FR-2019-02-07/pdf/2019-00936.pdf>.
- 882
- 883 (81) Environment and Climate Change Canada. *Evaluation of the Effectiveness of Risk*
884 *Management Measures for Mercury*; En14-411/2020E-PDF; 2020; pp 1–43.
885 [https://www.canada.ca/en/environment-climate-change/services/management-toxic-](https://www.canada.ca/en/environment-climate-change/services/management-toxic-substances/evaluation-effectiveness-risk-management-measures-mercury.html)
886 [substances/evaluation-effectiveness-risk-management-measures-mercury.html](https://www.canada.ca/en/environment-climate-change/services/management-toxic-substances/evaluation-effectiveness-risk-management-measures-mercury.html).
- 887 (82) Bruno, D. E.; De Simone, F.; Cinnirella, S.; Hedgecock, I. M.; D’Amore, F.; Pirrone, N.
888 Reducing Mercury Emission Uncertainty from Artisanal and Small-Scale Gold Mining
889 Using Bootstrap Confidence Intervals: An Assessment of Emission Reduction Scenarios.
890 *Atmosphere* **2022**, 14 (1), 62. <https://doi.org/10.3390/atmos14010062>.
- 891 (83) Mulvaney, K. M.; Selin, N. E.; Giang, A.; Muntean, M.; Li, C.-T.; Zhang, D.; Angot, H.;
892 Thackray, C. P.; Karplus, V. J. Mercury Benefits of Climate Policy in China: Addressing
893 the Paris Agreement and the Minamata Convention Simultaneously. *Environ. Sci. Technol.*
894 **2020**, 54 (3), 1326–1335. <https://doi.org/10.1021/acs.est.9b06741>.

- 895 (84) Rafaj, P.; Cofala, J.; Kuenen, J.; Wyrwa, A.; Zyśk, J. Benefits of European Climate Policies
896 for Mercury Air Pollution. *Atmosphere* **2014**, *5* (1), 45–59.
897 <https://doi.org/10.3390/atmos5010045>.
- 898 (85) Wohlgemuth, L.; Rautio, P.; Ahrends, B.; Russ, A.; Vesterdal, L.; Waldner, P.;
899 Timmermann, V.; Eickenscheidt, N.; Fürst, A.; Greve, M.; Roskams, P.; Thimonier, A.;
900 Nicolas, M.; Kowalska, A.; Ingerslev, M.; Merilä, P.; Benham, S.; Iacoban, C.; Hoch, G.;
901 Alewell, C.; Jiskra, M. Physiological and Climate Controls on Foliar Mercury Uptake by
902 European Tree Species. *Biogeosciences* **2022**, *19* (5), 1335–1353.
903 <https://doi.org/10.5194/bg-19-1335-2022>.
- 904 (86) COP26. *Glasgow Leaders' Declaration on Forests and Land Use*; 2021.
905 <https://ukcop26.org/glasgow-leaders-declaration-on-forests-and-land-use/>.
- 906 (87) Yuan, T.; Zhang, P.; Song, Z.; Huang, S.; Wang, X.; Zhang, Y. Buffering Effect of Global
907 Vegetation on the Air-Land Exchange of Mercury: Insights from a Novel Terrestrial
908 Mercury Model Based on CESM2-CLM5. *Environment International* **2023**, *174*, 107904.
909 <https://doi.org/10.1016/j.envint.2023.107904>.
- 910

1 **Supplementary Information (SI) for**
2 **Deforestation as an anthropogenic driver of mercury pollution**

3

4 Aryeh Feinberg^a, Martin Jiskra^b, Pasquale Borrelli^c, Jagannath Biswakarma^{b,d}, and Noelle E.
5 Selin^{a,e}

6 ^a *Institute for Data, Systems, and Society, Massachusetts Institute of Technology, Cambridge,*
7 *MA, USA*

8 ^b *Environmental Geosciences, University of Basel, Basel, Switzerland*

9 ^c *Department of Science, Roma Tre University, Rome, Italy*

10 ^d *Department of Water Resources and Drinking Water, Eawag, Dübendorf, Switzerland*

11 ^e *Department of Earth, Atmospheric, and Planetary Sciences, Massachusetts Institute of*
12 *Technology, Cambridge, MA, USA*

13 *Correspondence to: arifeinberg@gmail.com (A.F.); martin.jiskra@gmail.com (M.J.)

14

15

16 Section S1. Soil emissions parameterization

17 We improved the model's parametrization of Hg^0 soil emissions by adopting a new formulation for the
18 parametrization, suggested by Khan et al.¹:

$$19 \quad E_{\text{soil}} = aC^bR_g^c \quad (\text{Eq. S1})$$

20 where E_{soil} are soil emissions ($\text{ng m}^{-2}\text{h}^{-1}$), C is the concentration of Hg in soils (ng g^{-1}), R_g is the solar
21 radiation flux at the ground (W m^{-2}), and a , b , and c are coefficients.

22
23 As in Selin et al.², the solar radiation at ground (R_g) is determined by considering attenuation of the
24 solar radiation flux (R_s) by shading from the overhead canopy, parametrized by the leaf area index
25 (LAI):

$$26 \quad R_g = R_s \exp\left(-\frac{\alpha\text{LAI}}{\cos\theta}\right) \quad (\text{Eq. S2})$$

27 where $\alpha = 0.5$, assuming extinction from a random angular distribution of leaves³ and θ is the solar
28 zenith angle.

29
30 We compiled several relevant observational constraints for the parametrization in Tables S1 and S2.
31 Observational studies from the Amazon region suggest that deforestation has a large impact on soil
32 emissions due to removal of canopy shading, showing factors of 1.8×, 6.7×, and >31× more emissions
33 in forested compared to deforested land plots (Table S1). Observational studies from other regions
34 find a similarly high sensitivity of soil emissions to the presence of forest: open fields in China
35 showed 6–10 times higher Hg emissions than forests⁴ and logging in the US flipped the surface-air
36 Hg^0 flux from net deposition to net emissions ($-2.2 \mu\text{g m}^{-2}\text{yr}^{-1}$ to $+5.5 \mu\text{g m}^{-2}\text{yr}^{-1}$)⁵. For extratropical
37 grassland soil emissions, we use the compiled median values from Zhu et al.⁶ and Agnan et al.⁷

38
39 We conducted a parameter sweep of a , b , and c , calculating globally-gridded soil emissions using
40 annual solar radiation data (Fig. S1). Sensitivity simulations showed that the ratio of deforested to
41 forested soil emissions in the Amazon (median value 6.7) can tune the exponent for the radiation term
42 (c in Eq. S1), i.e., the response of emissions to canopy shading. The exponent for the soil
43 concentration term (b) was tuned with the ratio of deforested Amazon soil emissions (Table S1) to
44 extratropical grassland soil emissions from the Northern Hemisphere from two review studies^{6,7}
45 (overall Amazon to extratropical ratio of 5.3). Lastly, after these coefficients are tuned, the prefactor a
46 is adjusted so that predicted annual mean emissions match the observed median magnitudes of
47 Amazon deforested soil emissions ($23 \mu\text{g m}^{-2}\text{yr}^{-1}$) and extratropical grassland emissions ($4.3 \mu\text{g m}^{-2}$
48 yr^{-1}).

49
50 We recognize the uncertainties in the observed data used to tune this parametrization, and thus we
51 constructed 100 alternative parametrizations that fit within observed data bounds (Table S5). These
52 parametrizations were applied in offline uncertainty analyses to assess 95% confidence intervals in the
53 fluxes driven by deforestation (Section S4).

54
55

56 **Table S1.** Literature review of available Hg⁰ soil emission flux measurements from the Amazon
 57 region, differentiated by land cover type.

Reference	Location	Site	Deforested Hg ⁰ flux ($\mu\text{g m}^{-2} \text{yr}^{-1}$)	Forested Hg ⁰ flux ($\mu\text{g m}^{-2} \text{yr}^{-1}$)	Flux ratio (deforest:forest)
Magarelli and Fostier ⁸	Negro River Basin, Brazil	#1	27 ± 9	0.6 ± 1.5	
		#2	19	-1.0 ± 0.8	
		#3	9.8 ± 0.7		
		Mean	18	-0.2	> 31 ^a
Almeida et al. ⁹	Rondônia, Brazil	#1	79 ± 110	44 ± 18	1.8
Carpi et al. ¹⁰	Acre, Brazil	#1	19 ± 2	2.9 ± 0.8	6.7
		#2	230 ^b		
Median			23	1.8	6.7

58 ^alower limit calculated assuming the forested flux is equal to site #1, as site #2 shows negative overall flux;
 59 deforested flux assumed as mean.

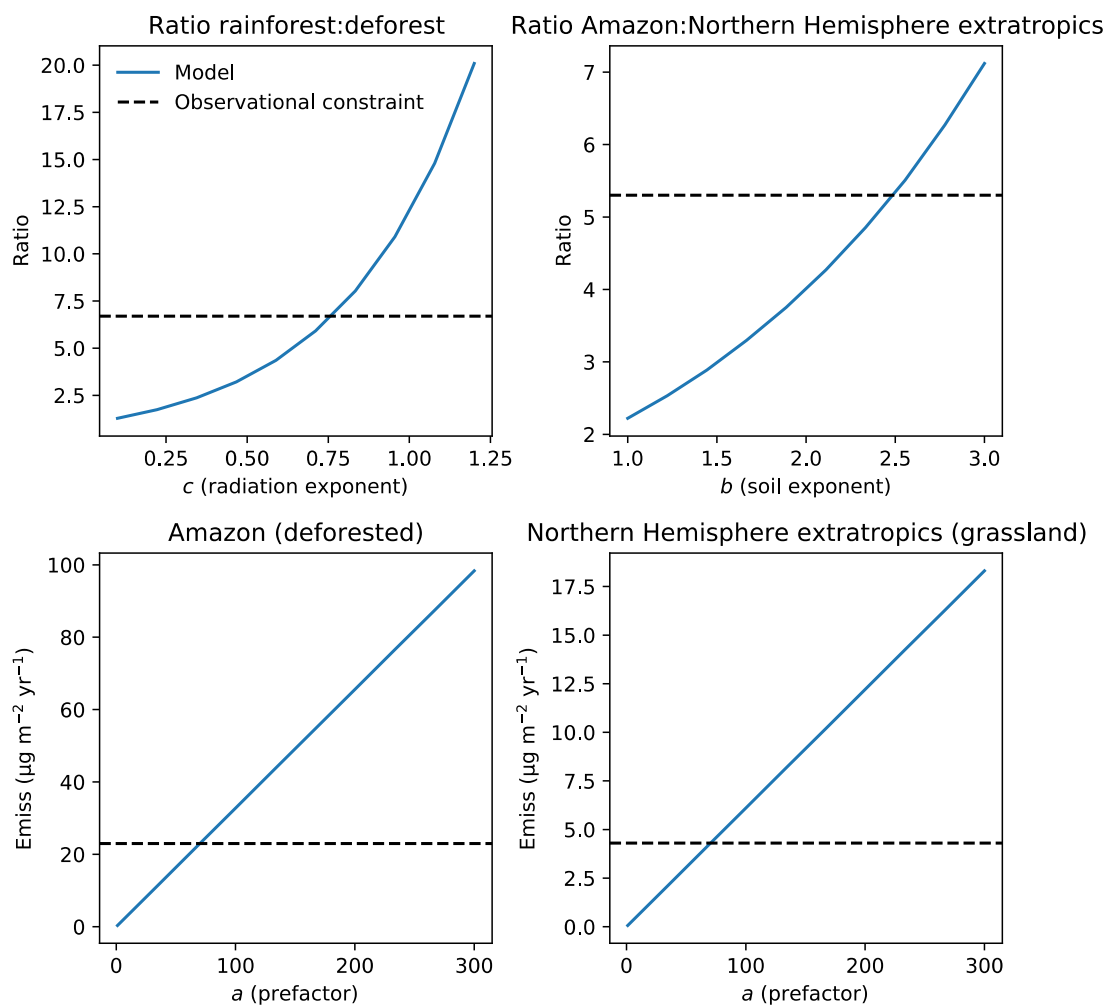
60 ^bthis site was 2-months post-fire and soil temperatures were still elevated; this flux is excluded from ratio
 61 calculations

62

63 **Table S2.** Observational constraints used to tune the soil emissions parametrization.

Constraint	Value	Reference	Coefficient constrained
Amazon deforested soil emissions ($\mu\text{g m}^{-2} \text{yr}^{-1}$)	23	Table S1	<i>a</i>
Extratropical grassland soil emissions ($\mu\text{g m}^{-2} \text{yr}^{-1}$)	4.3 [†]	Zhu et al. ⁶ ; Agnan et al. ⁷	<i>a</i>
Ratio of Amazon to extratropical soil emissions	5.3	(23:4.3)	<i>b</i>
Ratio of deforested to forested Amazon soil emissions	6.7	Table S1	<i>c</i>

64 [†]average of grassland median Hg⁰ fluxes from the two independent review studies



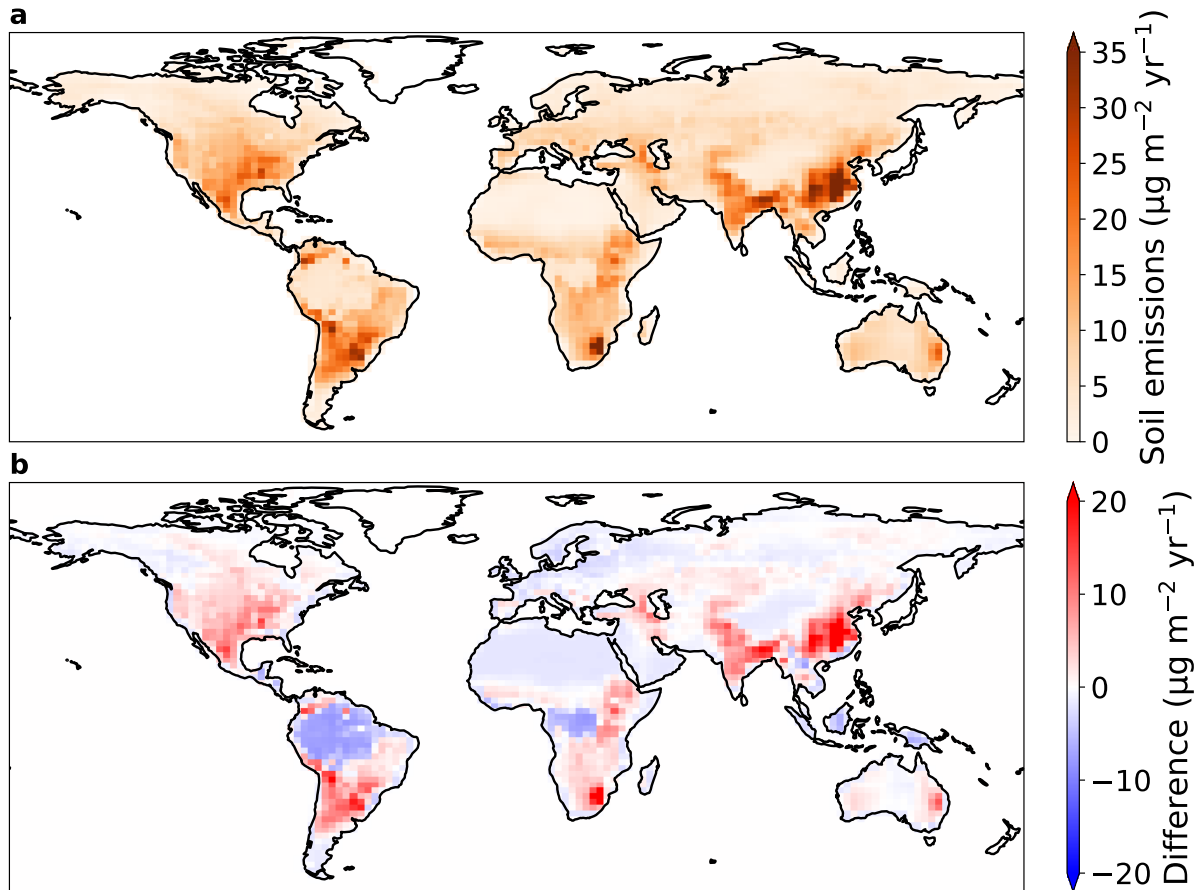
65

66 **Figure S1.** Parameter tuning (Eq. S1) to match observational constraints from Table S2.

67

68 The tuning procedure is illustrated in Fig. S1, yielding best matches for $a = 71$, $b = 2.5$, and
 69 $c = 0.76$. We compare the gridded annual mean soil emissions from the previous soil emission
 70 parametrization (GEOS-Chem v12.8) and the current study (Eq. S1) in Fig. S2. Global annual mean
 71 soil Hg^0 emissions in the new parametrizations (954 Mg yr^{-1}) is similar to the predictions from two
 72 GEOS-Chem studies^{11,12} using the previous parametrization: $860 \pm 440 \text{ Mg yr}^{-1}$ and 910 Mg yr^{-1} . The
 73 spatial distribution of emissions (Fig. S2) shows a decrease in vegetated regions (e.g., the Amazon and
 74 Congo rainforests) and an increase in regions with high soil Hg concentrations (e.g., eastern China).

75



76

77 **Figure S2.** (a) Annual mean soil emissions of Hg⁰ with the new parametrization. (b) Difference
78 between new and old (GEOS-Chem v12.8) soil emissions parametrizations (new minus old).
79

80 Section S2. Observational constraints on deforestation Hg fluxes

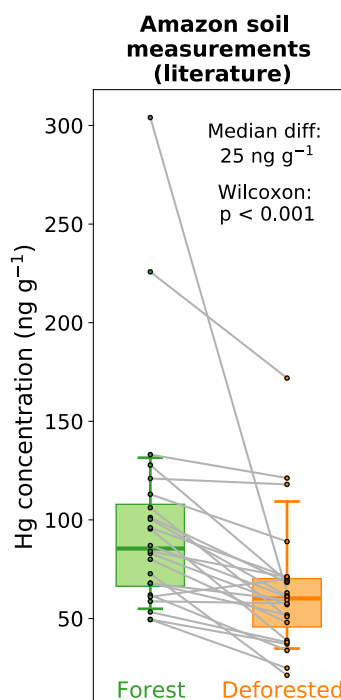
81 There are several available sources of information that can be used to validate the deforestation
82 emission factors (EF) calculated by GEOS-Chem (Fig. 1, SI Spreadsheet):
83

84 1) Soil Hg concentration measurements of paired forest-deforested sites:

85 Previous studies have measured the concentrations of Hg soils at deforested sites (C_d) and nearby
86 forest (C_f) plots. For this analysis, we assume that the difference in these soil concentrations is due to
87 mainly the change in atmospheric exchange, which is supported by the magnitude of modeled erosion
88 fluxes (Section S6) and available measurements⁵. We use the following equation to convert the
89 difference in these concentrations to a deforestation emission factor of Hg in Mg m⁻² yr⁻¹:

$$90 \text{ Total EF} = \frac{(C_d - C_f) \times \rho \times h}{t_d} \quad (\text{S3})$$

91 where ρ is the density of the soil, h is the depth of the soil layer, and t_d is the time since deforestation.
92 In the US (Nearctic), there have been studies in Ohio¹³ and Oregon¹⁴ with measurements of Hg in
93 deforested and forested soils, which we use to calculate deforestation EFs for the Nearctic. For the
94 Amazon, more measurements are available (24 pairs of soil plots)^{8-10,15-25}. We compiled a literature
95 database of studies that compared Hg concentrations in deforested Amazonian soils with nearby forest
96 plots (Fig. S3; SI Spreadsheet). Deforested sites show a consistent decrease compared to paired
97 forested sites (p -value < 0.001; Wilcoxon signed-rank test), with the median decrease being 25 ng g⁻¹
98 (10th-90th percentile: 2-58 ng g⁻¹). To calculate a deforestation EF for the Amazon, we apply this
99 concentration decrease in Eq. S3 and assume an average Amazon soil density of 1.25 ng g⁻¹, a surface
100 soil layer of 10 cm, and that deforested soils in the literature studies were measured 10 years after
101 deforestation.



102
 103 **Figure S3.** Measured Hg concentrations in forest (green) and deforested (orange) soils (0–20 cm
 104 depth) from the literature ($n = 24$)^{8–10,15–25}. Box plots show the median values (solid lines),
 105 interquartile range (shaded), and 10th and 90th percentiles (whiskers). Gray lines connect paired sites
 106 from the same study. Listed p -value (<0.001) refers to the Wilcoxon signed-rank test of the null
 107 hypothesis that paired forest and deforested sites come from the same distribution.

108
 109 2) *Terrestrial-atmosphere exchange models validated by Hg observations:*
 110 An estimate for the deforestation EF over China is available from the Wang et al.²⁶ modeling study.
 111 We use their area-averaged mean fluxes over forest and agricultural land cover to calculate a
 112 deforestation emission factor:

$$113 \quad \text{Total EF} = (E_d - D_d) - (E_f - D_f) \quad (\text{S4})$$

114 where E_d and E_f are the terrestrial emission fluxes ($\text{Mg m}^{-2} \text{yr}^{-1}$) from Chinese agricultural land and
 115 forest, and D_d and D_f are the deposition fluxes ($\text{Mg m}^{-2} \text{yr}^{-1}$) to Chinese agricultural land and forest.
 116 Although this EF estimate is model-based, the Wang et al.²⁶ model was validated extensively with
 117 available terrestrial-atmosphere exchange measurements from China.

118
 119 3) *Dynamic flux chamber measurements of forested and deforested soils:*
 120 Additional studies investigating the impact of deforestation on atmospheric fluxes quantified the
 121 response of soil emissions using dynamic flux chamber measurements^{5,8–10,27,28}. We compare these
 122 measurements to the soil-only EF modeled by GEOS-Chem. The soil emission factors measured by
 123 the studies is calculated as the difference between soil emissions ($\text{Mg m}^{-2} \text{yr}^{-1}$) over deforested and
 124 forested soils:

$$125 \quad \text{Soil EF} = E_d - E_f \quad (\text{S5})$$

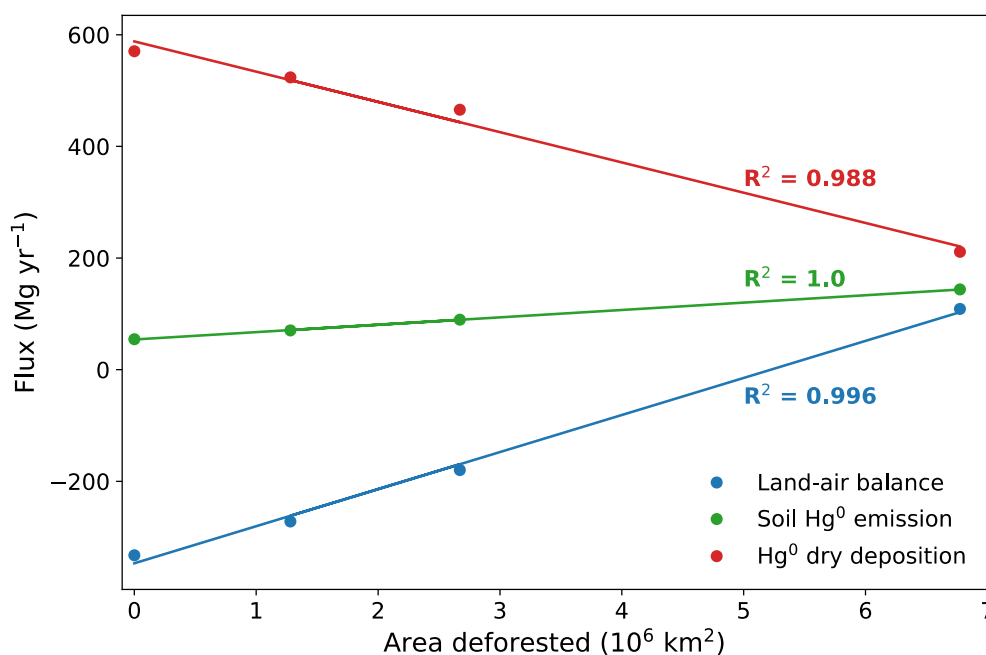
126
 127 The comparison between GEOS-Chem simulated deforestation EFs and observation-derived values is
 128 summarized in Fig. 1. Observations are only available from three regions (Amazon, China and
 129 Nearctic). We found further references investigating the impact of deforestation on Hg for the
 130 Palearctic region^{29,30}, yet these focused on measuring Hg concentrations in aquatic media and
 131 methylation potential rather than soil concentrations or atmospheric exchange. Australian soil
 132 measurements^{31,32} have been made before and after vegetation burning events, but do not cover the
 133 longer term soil Hg response to deforestation.

134
 135 The modeled EF estimates and their uncertainties overlap with observation-derived EFs for all 3
 136 regions. If anything, the modeled best estimate used in online simulations is conservative compared to

137 available observations, showing generally lower EFs (Fig. 1). However, it is unclear whether the
 138 sparse observations available are representative of the overall region. The modeled EF uncertainty
 139 estimates cover 1–2 orders of magnitude, emphasizing the current uncertainties in the response of Hg
 140 fluxes to deforestation. Figure 1 also reveals the regions where no observations of the impact of
 141 deforestation on Hg cycling are currently available. Specifically, the Afrotropic and Indomalayan
 142 domains would be priorities for future measurement campaigns, given the current impact of
 143 deforestation in those regions (Fig. 2). It remains unknown whether Southeast Asian and African
 144 rainforests show similarly high levels of Hg in litterfall as the Amazon rainforest³³.

146 Section S3. Global deforestation-driven emissions estimates

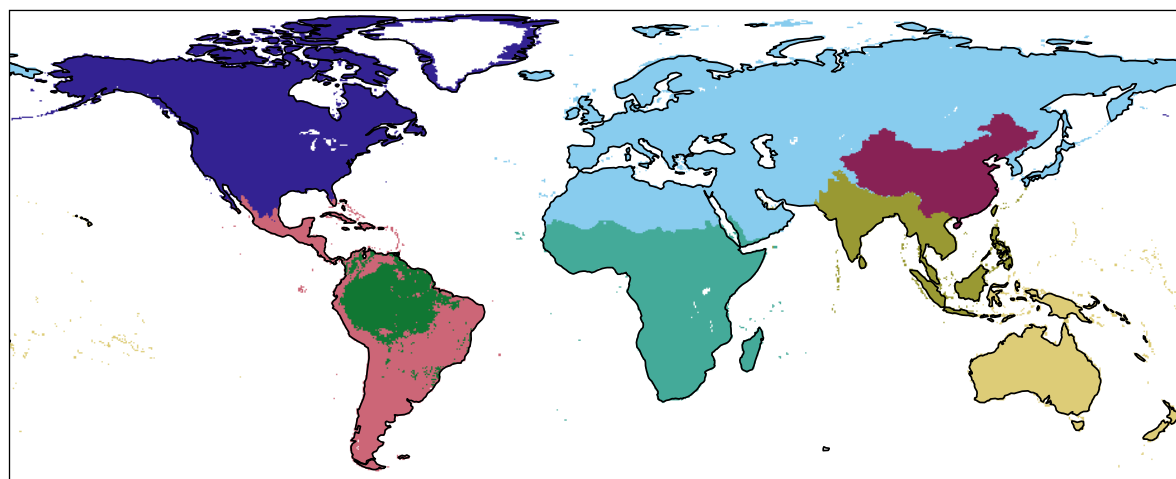
147 We use perturbation simulations in which a set area within each region is deforested to calculate each
 148 deforestation EF. In the EF approach, we assume that 1) land-air fluxes respond linearly to deforested
 149 area and 2) spatial variability in the deforestation response within regions can be ignored. We explored
 150 the validity these assumptions using the four Amazon deforestation scenario simulations conducted in
 151 this work (Fig. S4). In the Amazon simulations — the reference simulation with 2003 forest cover
 152 (HIST), governance scenario for 2050 (GOV), business-as-usual for 2050 (BAU), and savannization
 153 (SAV) — different areas (both in spatial pattern and extent) were deforested in the Amazon region.
 154 The total fluxes from the Amazon basin for Hg⁰ dry deposition, soil Hg⁰ emissions, and the overall
 155 land-air balance of Hg all respond linearly ($R^2 > 0.98$) to the magnitude of the deforested area.
 156 Therefore, the approach of calculating deforestation EFs and scaling these with deforested areas would
 157 likely not be highly sensitive to the spatial distribution and amount of deforestation. Therefore, we
 158 conducted 7 other idealized deforestation simulations for the other land regions (Fig. S5).



160
 161 **Figure S4.** Relationship between land-air fluxes and the area deforested in GEOS-Chem simulations
 162 for the Amazon rainforest. Fluxes are averaged over the Amazon rainforest domain and listed R^2
 163 values refer to linear models.

164
 165 Additional data related to the calculation of historical deforestation-driven emissions of Hg are
 166 presented in this section. The maps defining the regions used in this study is shown in Fig. S5. Table
 167 S3 tabulates the results from the perturbation simulations for the different regions and the resultant
 168 emission factors. Fig. S6 explores the impact of choosing different time horizons for the deforestation
 169 area on the calculated Hg emissions globally and by country. Fig. S7 shows the map of Hg
 170 deforestation-driven emissions, assuming a 45 year time horizon (deforestation area of 1970–2014
 171 from the LUH2 dataset³⁴).

172



■ Palearctic
 ■ Nearctic
 ■ China
 ■ Australasia & Oceania
■ Afrotropic
 ■ Indomalaya
 ■ Amazon
 ■ Neotropic

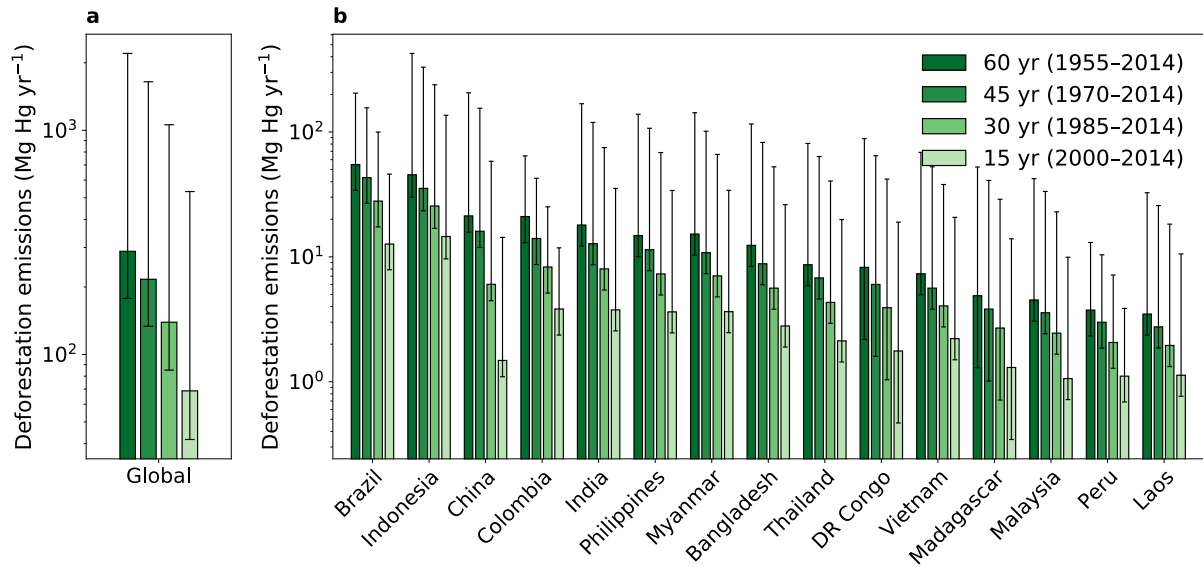
173
174
175
176
177
178
179
180
181

Figure S5. Definition of regions used to calculate the deforestation emission factors.

Table S3. Results from the deforestation perturbation simulations in GEOS-Chem for determining the response of land-air fluxes to deforesting a specified area. Emissions factors are listed with the 95% confidence interval calculated in offline simulations assessing the uncertainties due to model parameters (Section S4).

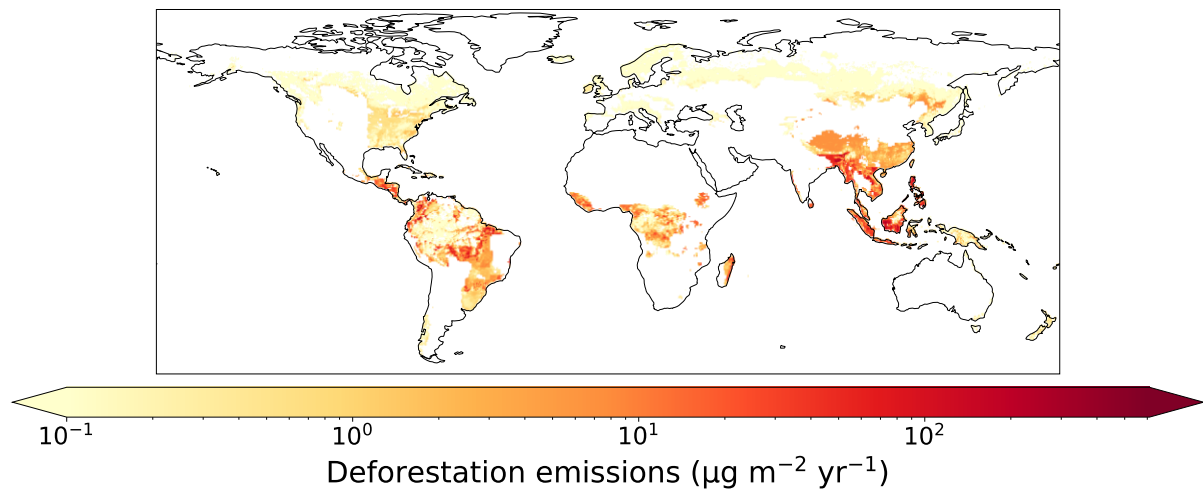
Realm	Area deforested (km ²)	Change in emissions (Mg yr ⁻¹)	Change in deposition (Mg yr ⁻¹)	Change in net emissions (Mg yr ⁻¹)	Emissions factor (Mg m ⁻² yr ⁻¹) [95% confidence interval]
Afrotropic	3 644 969	29.1	-10.0	39.1	1.1×10^{-5} [2.8×10^{-6} to 1.2×10^{-4}]
Neotropic	2 422 577	13.0	-4.9	17.9	7.4×10^{-6} [4.8×10^{-6} to 5.7×10^{-5}]
Indomalaya	2 626 474	31.6	-28.3	59.9	2.3×10^{-5} [1.5×10^{-5} to 2.1×10^{-4}]
Palearctic	4 221 663	5.8	-4.3	10.1	2.4×10^{-6} [7.6×10^{-8} to 2.3×10^{-5}]
Nearctic	4 606 898	31.6	-17.4	48.9	1.1×10^{-5} [7.1×10^{-6} to 6.2×10^{-5}]
Australasia	1 088 250	1.9	-4.8	6.6	6.1×10^{-6} [8.3×10^{-7} to 5.4×10^{-5}]
China	1 141 180	16.6	-10.1	26.7	2.3×10^{-5} [1.7×10^{-5} to 2.3×10^{-4}]
Amazon	6 775 429	96.2	-394.0	490.2	7.2×10^{-5} [4.5×10^{-5} to 2.0×10^{-4}]

182



183

184 **Figure S6.** (a) Global and (b) country-level deforestation emissions of Hg for the top 15 emitting
 185 countries. Results are summarized accumulating deforested area over different time horizons (15
 186 years, 30 years, 45 years, and 60 years) before 2015. Error bars refer to the 95% confidence interval
 187 based on the uncertainty in model parameters (Section S4).
 188



189

190 **Figure S7.** Map of net emissions of Hg from deforestation calculated over a 45 year time horizon
 191 before 2015 (1970–2014), using deforested area from the LUH2 dataset³⁴.
 192

193

194 **Section S4. Model uncertainty analysis**

195

196 **Table S4.** Parameter uncertainty bounds applied in the uncertainty analysis.

Parameter	Min	Max	Units	Distribution	Comment
Soil emission parametrization	1	100	-	Uniform	Integer representing one of 100 reasonable parametrizations calculated within the range of observed uncertainties (Table S5)
Percentile of replaced LAI when building scenarios	10	90	-	Uniform	e.g., deforested Amazon area is assigned 10 th percentile LAI of HIST savanna, instead of mean for default estimate
Dry deposition Hg ⁰ reactivity (f_0) Amazon rainforest	10 ⁻²	0.5	-	Loguniform	Based on Feinberg et al. ³³ , within range of available vegetation uptake measurements
Dry deposition Hg ⁰ reactivity (f_0) other rainforests	10 ⁻⁵	0.2	-	Loguniform	Based on Feinberg et al. ³³ ; no available measurements from other rainforests, leading to wider f_0 uncertainty
Dry deposition Hg ⁰ reactivity (f_0) elsewhere	10 ⁻⁵	5 × 10 ⁻⁵	-	Uniform	Based on Feinberg et al. ³³ , within range of available vegetation uptake measurements
Biomass burning emission factor for Amazon	350	615	µg m ⁻²	Uniform	Estimated range in literature ^{10,35,36}

197

198

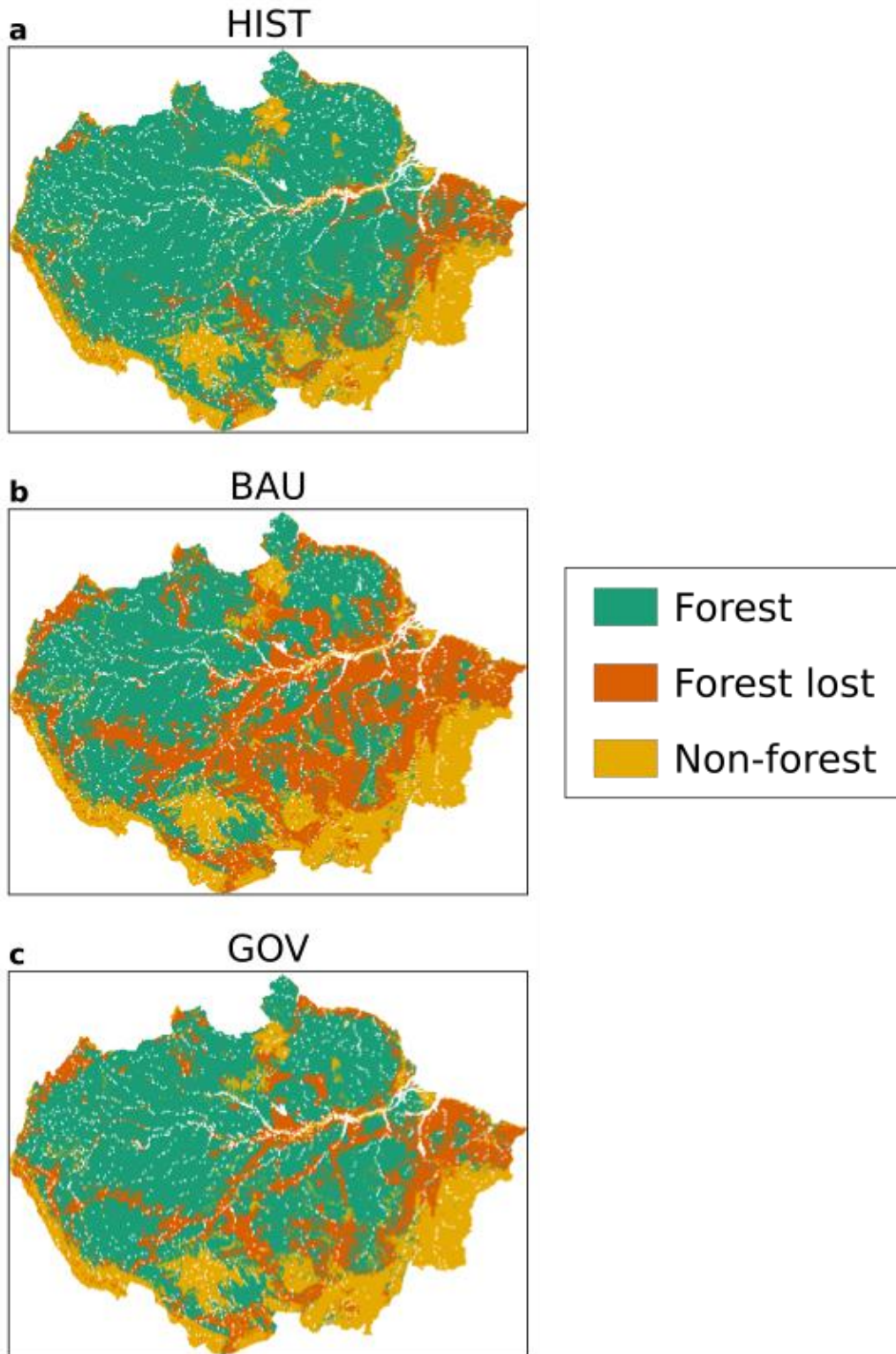
199 **Table S5.** Bounds of observed parameters used to calculate 100 reasonable soil emission
200 parametrizations, which are then applied in the uncertainty analysis (Table S4).

Parameter	Min	Max	Units	Comment
Ratio of deforested to forested Amazon soil emissions	1.8	31	-	Range from Table S1
Ratio of Amazon to extratropical soil emissions	3.5	8	-	Assume 50% error from Table S2
Extratropical grassland soil emissions	3.5	11.4	µg m ⁻² yr ⁻¹	Grasslands and background soil range from literature reviews ^{6,7}
Deforested Amazon soil emissions	9.8	79	µg m ⁻² yr ⁻¹	Range from Table S1

201

202

203 Section S5. Scenarios for Amazon deforestation and global reforestation

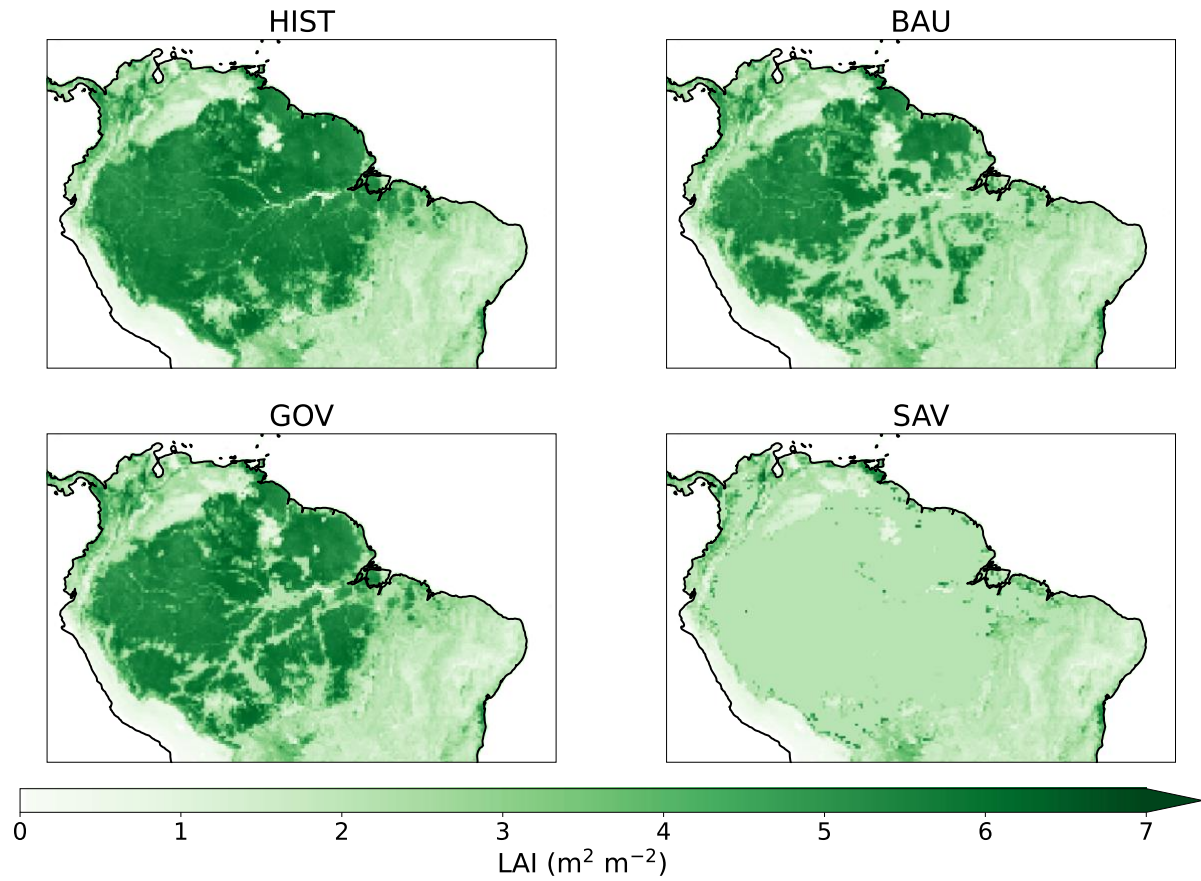


204

205 **Figure S8.** Map of the Amazon basin showing the area of forest, forest loss and rangeland and
 206 agriculture in (a) HIST; and projections for 2050 in (b) Business as Usual (BAU) and (c) Governance
 207 (GOV) scenarios (replotted from Soares-Filho et al.³⁷ data).

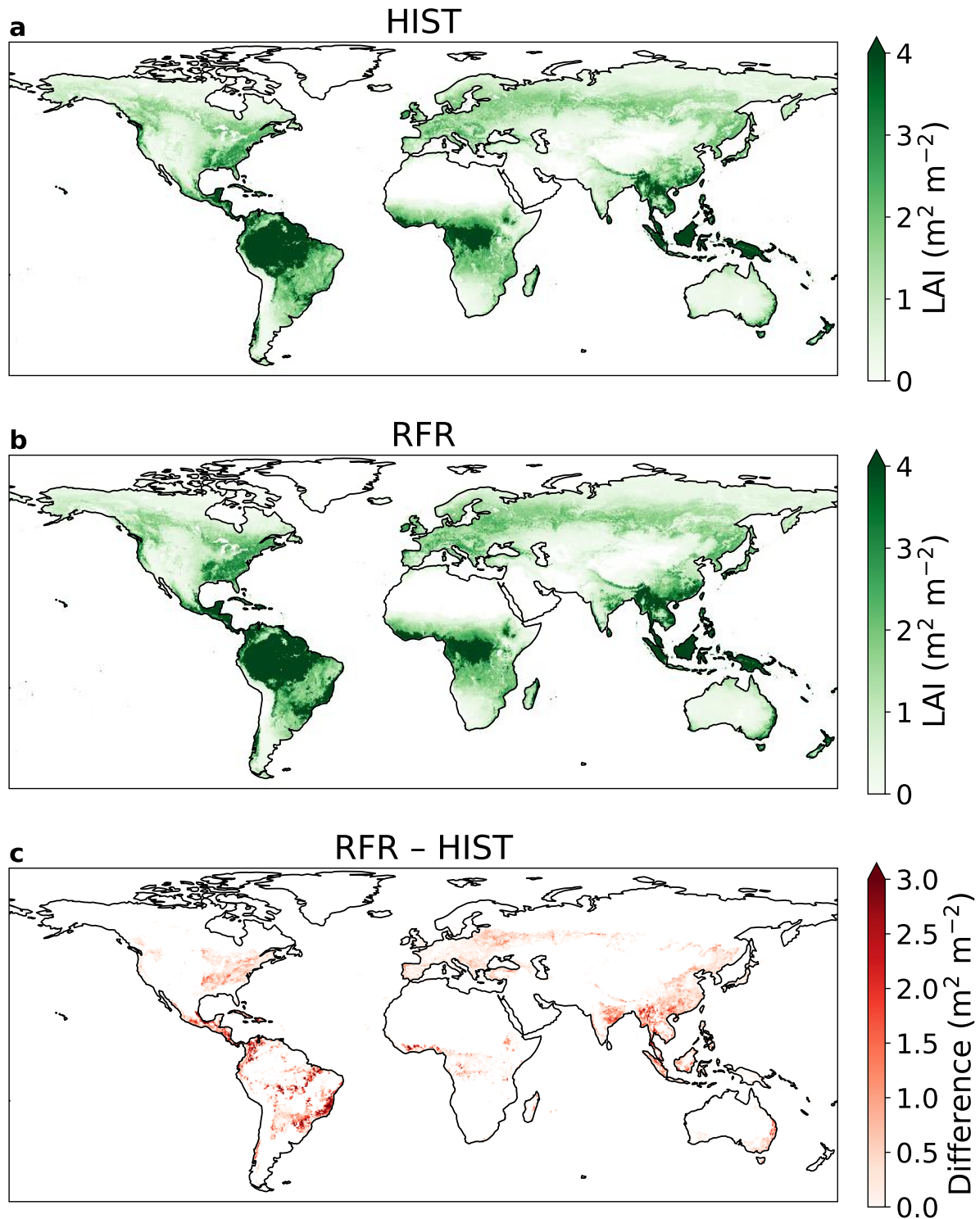
208

209



210

211 **Figure S9.** Annual mean leaf area index (LAI) maps for the Amazon deforestation scenarios at 0.25°
212 $\times 0.25^\circ$ resolution. The simulations names refer to the following scenarios: reference (HIST),
213 Business-as-usual (BAU), Governance (GOV), and Savannization (SAV).



214

215 **Figure S10.** Annual mean leaf area index (LAI) maps at $0.25 \times 0.25^\circ$ resolution for: (a) the reference
 216 (HIST) scenario (b) Reforestation scenario (RFR) (c) Difference between RFR and HIST.

217

218 **Section S6. Impact of Amazon deforestation on erosion**

219 Previous field studies^{15,38} have suggested that erosion of Hg is increased after deforestation in the
 220 Amazon, measuring enhanced runoff of Hg in deforested catchments. We estimated the change in soil
 221 displacement by water erosion (soil erosion) in the Amazon deforestation scenarios using the RUSLE-
 222 based³⁹ modeling platform Global Soil Erosion Modeling (GloSEM)^{40,41}. As a detachment-limited soil
 223 erosion prediction model, GloSEM estimates soil erosion (expressed as a mass of soil lost per unit area
 224 and time, $\text{Mg ha}^{-1} \text{yr}^{-1}$) due to inter-rill and rill erosion processes by multiplication of six contributing

225 factors. The modeling scheme follows the same principle of most RUSLE-type models or more
 226 complex catchment-scale process-based models, with a driving force (erosivity of the climate, R), a
 227 resistance term (erodibility of the soil, K) and other factors representing the farming choice, i.e.,
 228 topographical conformation of the field (LS), cropping system (C), and soil conservation practices (P).
 229

230 Our approach for calculating soil erosion in the Amazon scenarios is similar to the GloSEM
 231 parametrization adopted by Borrelli et al.^{40,41} to estimate human-induced soil erosion change between
 232 2001 and 2070 at a global scale. The horizontal resolution of the native soil erosion modeling is 250 ×
 233 250 m. The calculation of erosivity (R), erodibility (K), topographical conformation of the field (LS),
 234 and soil conservation practices (P) factors are described in Borrelli et al.^{40,41}. We acknowledge that the
 235 calculation of erosion model factors for the Amazon rainforest may be associated with higher
 236 uncertainties than other regions due to the lower density in meteorological stations⁴² and soil sampling
 237 sites⁴³. For this study, we adapted the computation of the land cover and management factor (C-
 238 factor), which measures the combined effect of vegetation cover and cropping system variables on the
 239 soil erosion process. We parametrize the C-factor according to two layers of information: 1) the spatial
 240 dimension of land use classes according to the deforestation scenarios from Soares-Filho et al.³⁷
 241 (described below); 2) the vegetation condition in each land use class using the MODIS MOD44B
 242 Vegetation Continuous Fields product (VCF) (~250m spatial resolution) as a proxy to quantify (i)
 243 surface vegetation cover, (ii) tree cover, and (iii) bare soil. As we focus our analysis on comparing the
 244 forest coverage in the years 2003 and 2050, the baseline vegetation condition is given by the average
 245 VCF values over the years 2000, 2001 and 2002. The C-factor for noncropland areas (C_{nc}) is estimated
 246 in two steps. First, a preliminary C-factor (C_p) not considering tree cover is calculated as:

$$247 \quad C_p = C_{min} + ((C_{max} - C_{min}) NVS) \quad (S6)$$

248 where the C_{min} (0.01) and C_{max} (0.15) express the potential range in C-factor values for dense to
 249 sparse grassland cover. NVS (non-vegetated surface) is spatially defined using the MODIS MOD44B
 250 VCF data normalized to a range from 0 to 1 and describes the percentage of ground covered by any
 251 vegetation type. For the NVS, the C-factor is set to 0.5. Within the next step, the final land cover and
 252 management C-factor for non-croplands (C_{nc}) is computed including the tree coverage (TC) defined
 253 using the MODIS MOD44B VCF normalized to range from 0 to 1:

$$254 \quad C_{nc} = C_{p\ min} + ((C_{p\ max} - C_{p\ min}) TC) \quad (S7)$$

255 where the $C_{p\ min}$ and $C_{p\ max}$ values are set to 0.0001 (100% canopy cover) and 0.009 (sparse forest
 256 vegetation).

257
 258 While the deforestation scenarios proposed by Soares-Filho et al.³⁷ provide a spatial quantification of
 259 the forest losses between 2003 and 2050, the annual shares of conversion from forest to grassland or
 260 cropland are separate from the annual projection of the Land-Use Harmonization (LUH2) data³⁴,
 261 which provides fractional land-use patterns (850-2100) at $0.25^\circ \times 0.25^\circ$ resolution. The downscaling
 262 of the LUH2 fractional cropland and grassland data from $0.25^\circ \times 0.25^\circ$ resolution to the 250 m × 250
 263 m resolution of the erosion model is performed through a probabilistic land use allocation scheme
 264 based on classification rules applied to auxiliary information (i.e., a crop suitability index, more detail
 265 in Borrelli et al.⁴⁰). Finally, the C-factor of the cropland is defined at sub-national administrative level
 266 (Global Administrative Unit Levels) based on the Food and Agriculture Organization's (FAO)
 267 FAOSTAT database, which allowed to statistically describe typical crop rotations in each region. The
 268 C-factor of the croplands ranges from 0.131 (Northern Suriname) to 0.332 (Northeast Brazil).
 269

270 Following the assumption of Lugato et al.⁴⁴ for eroded carbon, we assume that 30% of the eroded soil
 271 flux is not redeposited on land and enters riverine systems. The fraction of eroded Hg which enters
 272 aquatic systems is uncertain, depending on hillslopes dynamics and flow patterns that are not
 273 explicitly modeled by the RUSLE-based framework, as well as whether Hg would be selectively
 274 eroded relative to carbon. We recognize that this assumption introduces uncertainty into our
 275 calculations, and assume that the fraction of eroded soil which enters riverine systems can vary
 276 between 5–47%, the range reported by Van Oost et al.⁴⁵ We calculate the eroded flux of Hg from land
 277 by multiplying the soil flux by the median Hg concentration in Amazon forested soils from a literature
 278 review (86 ng g⁻¹; see SI Spreadsheet).
 279

280 For each Amazon scenario, we tabulate the Hg erosion fluxes in Table S6. Erosion in the HIST
 281 scenario represents a flux of 64 Mg yr⁻¹ (uncertainty range: 11–100 Mg yr⁻¹). Erosion is enhanced in
 282 the deforestation scenarios, ranging from +14% increase in GOV to a 96% increase in the extreme
 283 SAV scenario. The absolute magnitudes of erosion flux changes are smaller than the perturbations in
 284 the land-air flux, driven by changes in Hg⁰ soil emissions and dry deposition (Table S6). Overall,
 285 perturbations to the erosion flux are approximately 14% of the perturbations to the land-air flux due to
 286 deforestation. A previous field study⁵ has also suggested that the majority of flux changes after
 287 deforestation occurs through atmospheric exchange (97%) rather than erosion to riverine systems.
 288 Therefore, the land-air changes to the fluxes play the larger role in the impact of deforestation on the
 289 mass balance of Hg in soils. Nevertheless, changes to erosion will affect downstream Hg
 290 concentrations and the methylation potential after deforestation^{5,29}, which would be important to
 291 consider when assessing the impact of deforestation on local ecosystems.

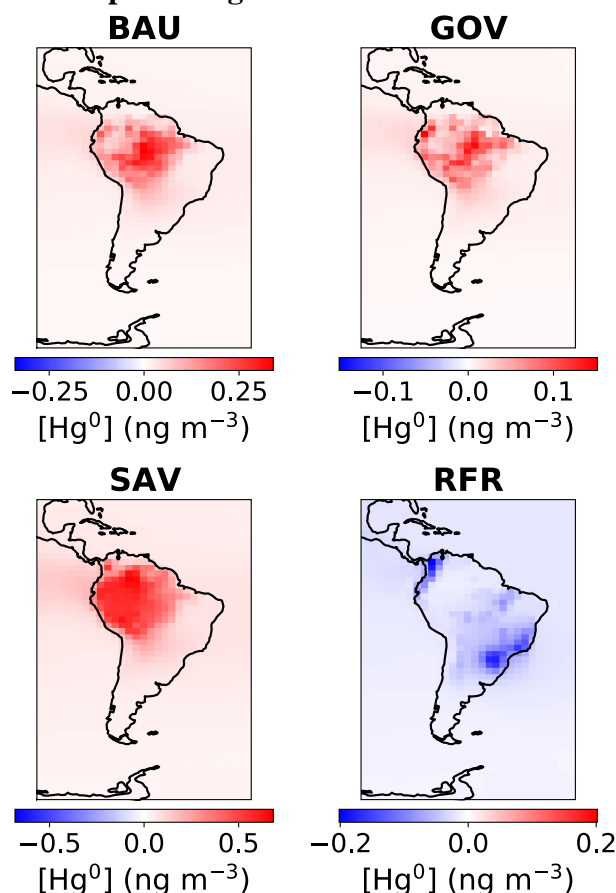
293 **Table S6.** Soil erosion fluxes for the Amazon basin calculated by the erosion model GloSEM. The
 294 simulations names refer to the following scenarios: reference (HIST), Business-as-usual (BAU),
 295 Governance (GOV), and Savannization (SAV).

Scenario	HIST	BAU	GOV	SAV
Soil loss (Mt yr ⁻¹)	2467	3276	2816	4834
30% of soil loss (Mt yr ⁻¹) ^a	740	983	845	1450
[5%–47%]	[123–1159]	[164–1540]	[141–1323]	[242–2272]
Hg erosion (Mg yr ⁻¹)	64	85	73	125
[uncertainty range]	[11–100]	[14–132]	[12–114]	[21–195]
Change from HIST (Mg yr ⁻¹)	-	21	9	61
(relative change)		(+33%)	(+14%)	(+96%)
Land-air flux change from HIST (Mg yr ⁻¹)	-	153	61	441

296 ^a This is the flux assumed to be entering riverine systems

297
 298

299 Section S7. Impacts on atmospheric Hg concentrations



300
 301 **Figure S11.** Annual mean differences in simulated atmospheric Hg^0 concentration at the surface
 302 between scenarios — Business-as-usual (BAU), Governance (GOV), Savannization (SAV), and global
 303 reforestation (RFR) — and the HIST reference simulation.

304

305 **Supplementary References**

- 306 (1) Khan, T. R.; Obrist, D.; Agnan, Y.; Selin, N. E.; Perlinger, J. A. Atmosphere-Terrestrial Exchange
 307 of Gaseous Elemental Mercury: Parameterization Improvement through Direct Comparison with
 308 Measured Ecosystem Fluxes. *Environ. Sci.: Processes Impacts* **2019**, *21* (10), 1699–1712.
 309 <https://doi.org/10.1039/C9EM00341J>.
- 310 (2) Selin, N. E.; Jacob, D. J.; Yantosca, R. M.; Strode, S.; Jaeglé, L.; Sunderland, E. M. Global 3-D
 311 Land-Ocean-Atmosphere Model for Mercury: Present-Day versus Preindustrial Cycles and
 312 Anthropogenic Enrichment Factors for Deposition. *Global Biogeochem. Cycles* **2008**, *22* (2),
 313 GB2011. <https://doi.org/10.1029/2007GB003040>.
- 314 (3) Verstraete, M. M. Radiation Transfer in Plant Canopies: Transmission of Direct Solar Radiation
 315 and the Role of Leaf Orientation. *J. Geophys. Res.* **1987**, *92* (D9), 10985.
 316 <https://doi.org/10.1029/JD092iD09p10985>.
- 317 (4) Zhou, J.; Wang, Z.; Zhang, X.; Driscoll, C. T.; Lin, C.-J. Soil–Atmosphere Exchange Flux of
 318 Total Gaseous Mercury (TGM) at Subtropical and Temperate Forest Catchments. *Atmos. Chem.*
 319 *Phys.* **2020**, *20* (24), 16117–16133. <https://doi.org/10.5194/acp-20-16117-2020>.
- 320 (5) Eckley, C. S.; Eagles-Smith, C.; Tate, M. T.; Krabbenhoft, D. P. Surface–Air Mercury Fluxes and
 321 a Watershed Mass Balance in Forested and Harvested Catchments. *Environmental Pollution*
 322 **2021**, *277*, 116869. <https://doi.org/10.1016/j.envpol.2021.116869>.
- 323 (6) Zhu, W.; Lin, C.-J.; Wang, X.; Sommar, J.; Fu, X.; Feng, X. Global Observations and Modeling
 324 of Atmosphere–Surface Exchange of Elemental Mercury: A Critical Review. *Atmos. Chem.*
 325 *Phys.* **2016**, *16* (7), 4451–4480. <https://doi.org/10.5194/acp-16-4451-2016>.

- 326 (7) Agnan, Y.; Le Dantec, T.; Moore, C. W.; Edwards, G. C.; Obrist, D. New Constraints on
327 Terrestrial Surface–Atmosphere Fluxes of Gaseous Elemental Mercury Using a Global
328 Database. *Environ. Sci. Technol.* **2016**, *50* (2), 507–524. <https://doi.org/10.1021/acs.est.5b04013>.
- 329 (8) Magarelli, G.; Fostier, A. Influence of Deforestation on the Mercury Air/Soil Exchange in the
330 Negro River Basin, Amazon. *Atmos. Environ.* **2005**, *39* (39), 7518–7528.
331 <https://doi.org/10.1016/j.atmosenv.2005.07.067>.
- 332 (9) Almeida, M. D.; Marins, R. V.; Paraquetti, H. H. M.; Bastos, W. R.; Lacerda, L. D. Mercury
333 Degassing from Forested and Open Field Soils in Rondônia, Western Amazon, Brazil.
334 *Chemosphere* **2009**, *77* (1), 60–66. <https://doi.org/10.1016/j.chemosphere.2009.05.018>.
- 335 (10) Carpi, A.; Fostier, A. H.; Orta, O. R.; dos Santos, J. C.; Gittings, M. Gaseous Mercury Emissions
336 from Soil Following Forest Loss and Land Use Changes: Field Experiments in the United States
337 and Brazil. *Atmos. Environ.* **2014**, *96*, 423–429. <https://doi.org/10.1016/j.atmosenv.2014.08.004>.
- 338 (11) Song, S.; Selin, N. E.; Soerensen, A. L.; Angot, H.; Artz, R.; Brooks, S.; Brunke, E.-G.; Conley,
339 G.; Dommergue, A.; Ebinghaus, R.; Holsen, T. M.; Jaffe, D. A.; Kang, S.; Kelley, P.; Luke, W.
340 T.; Magand, O.; Marumoto, K.; Pfaffhuber, K. A.; Ren, X.; Sheu, G.-R.; Slemr, F.; Warneke, T.;
341 Weigelt, A.; Weiss-Penzias, P.; Wip, D. C.; Zhang, Q. Top-down Constraints on Atmospheric
342 Mercury Emissions and Implications for Global Biogeochemical Cycling. *Atmos. Chem. Phys.*
343 **2015**, *15* (12), 7103–7125. <https://doi.org/10.5194/acp-15-7103-2015>.
- 344 (12) Horowitz, H. M.; Jacob, D. J.; Zhang, Y.; Dibble, T. S.; Slemr, F.; Amos, H. M.; Schmidt, J. A.;
345 Corbitt, E. S.; Marais, E. A.; Sunderland, E. M. A New Mechanism for Atmospheric Mercury
346 Redox Chemistry: Implications for the Global Mercury Budget. *Atmos. Chem. Phys.* **2017**, *17*
347 (10), 6353–6371. <https://doi.org/10.5194/acp-17-6353-2017>.
- 348 (13) Gamby, R. L.; Hammerschmidt, C. R.; Costello, D. M.; Lamborg, C. H.; Runkle, J. R.
349 Deforestation and Cultivation Mobilize Mercury from Topsoil. *Science of The Total*
350 *Environment* **2015**, *532*, 467–473. <https://doi.org/10.1016/j.scitotenv.2015.06.025>.
- 351 (14) Homann, P. S.; Darbyshire, R. L.; Bormann, B. T.; Morrisette, B. A. Forest Structure Affects
352 Soil Mercury Losses in the Presence and Absence of Wildfire. *Environ. Sci. Technol.* **2015**, *49*
353 (21), 12714–12722. <https://doi.org/10.1021/acs.est.5b03355>.
- 354 (15) Fostier, A. H.; Forti, M. C.; Guimarães, J. R.; Melfi, A. J.; Boulet, R.; Espirito Santo, C. M.;
355 Krug, F. J. Mercury Fluxes in a Natural Forested Amazonian Catchment (Serra Do Navio,
356 Amapá State, Brazil). *Sci. Total Environ.* **2000**, *260* (1–3), 201–211.
357 [https://doi.org/10.1016/S0048-9697\(00\)00564-7](https://doi.org/10.1016/S0048-9697(00)00564-7).
- 358 (16) Gerson, J. R.; Szponar, N.; Zambrano, A. A.; Bergquist, B.; Broadbent, E.; Driscoll, C. T.;
359 Erkenswick, G.; Evers, D. C.; Fernandez, L. E.; Hsu-Kim, H.; Inga, G.; Lansdale, K. N.;
360 Marchese, M. J.; Martinez, A.; Moore, C.; Pan, W. K.; Purizaca, R. P.; Sánchez, V.; Silman, M.;
361 Ury, E. A.; Vega, C.; Watsa, M.; Bernhardt, E. S. Amazon Forests Capture High Levels of
362 Atmospheric Mercury Pollution from Artisanal Gold Mining. *Nat Commun* **2022**, *13* (1), 559.
363 <https://doi.org/10.1038/s41467-022-27997-3>.
- 364 (17) Almeida, M. D.; Lacerda, L. D.; Bastos, W. R.; Herrmann, J. C. Mercury Loss from Soils
365 Following Conversion from Forest to Pasture in Rondônia, Western Amazon, Brazil.
366 *Environmental Pollution* **2005**, *137* (2), 179–186. <https://doi.org/10.1016/j.envpol.2005.02.026>.
- 367 (18) Lacerda, L. D.; de Souza, M.; Ribeiro, M. G. The Effects of Land Use Change on Mercury
368 Distribution in Soils of Alta Floresta, Southern Amazon. *Environmental Pollution* **2004**, *129* (2),
369 247–255. <https://doi.org/10.1016/j.envpol.2003.10.013>.
- 370 (19) Béliveau, A.; Lucotte, M.; Davidson, R.; do Canto Lopes, L. O.; Paquet, S. Early Hg Mobility in
371 Cultivated Tropical Soils One Year after Slash-and-Burn of the Primary Forest, in the Brazilian
372 Amazon. *Science of The Total Environment* **2009**, *407* (15), 4480–4489.
373 <https://doi.org/10.1016/j.scitotenv.2009.04.012>.
- 374 (20) Béliveau, A.; Lucotte, M.; Davidson, R.; Paquet, S.; Mertens, F.; Passos, C. J.; Romana, C. A.
375 Reduction of Soil Erosion and Mercury Losses in Agroforestry Systems Compared to Forests
376 and Cultivated Fields in the Brazilian Amazon. *Journal of Environmental Management* **2017**,
377 *203*, 522–532. <https://doi.org/10.1016/j.jenvman.2017.07.037>.
- 378 (21) Patry, C.; Davidson, R.; Lucotte, M.; Béliveau, A. Impact of Forested Fallows on Fertility and
379 Mercury Content in Soils of the Tapajós River Region, Brazilian Amazon. *Science of The Total*
380 *Environment* **2013**, *458–460*, 228–237. <https://doi.org/10.1016/j.scitotenv.2013.04.037>.

- 381 (22)Comte, I.; Lucotte, M.; Davidson, R.; Reis de Carvalho, C. J.; de Assis Oliveira, F.; Rousseau, G.
382 X. Impacts of Land Uses on Mercury Retention in Long-Time Cultivated Soils, Brazilian
383 Amazon. *Water Air Soil Pollut* **2013**, 224 (4), 1515. <https://doi.org/10.1007/s11270-013-1515-3>.
384 (23)Mainville, N.; Webb, J.; Lucotte, M.; Davidson, R.; Betancourt, O.; Cueva, E.; Mergler, D.
385 Decrease of Soil Fertility and Release of Mercury Following Deforestation in the Andean
386 Amazon, Napo River Valley, Ecuador. *Science of The Total Environment* **2006**, 368 (1), 88–98.
387 <https://doi.org/10.1016/j.scitotenv.2005.09.064>.
388 (24)Roulet, M.; Lucotte, M.; Saint-Aubin, A.; Tran, S.; Rhéault, I.; Farella, N.; De Jesus Da Silva, E.;
389 Dezencourt, J.; Sousa Passos, C.-J.; Santos Soares, G.; Guimarães, J.-R. D.; Mergler, D.;
390 Amorim, M. The Geochemistry of Mercury in Central Amazonian Soils Developed on the Alter-
391 Do-Chão Formation of the Lower Tapajós River Valley, Pará State, Brazil. *Science of The Total*
392 *Environment* **1998**, 223 (1), 1–24. [https://doi.org/10.1016/S0048-9697\(98\)00265-4](https://doi.org/10.1016/S0048-9697(98)00265-4).
393 (25)Wasserman, J. C.; Campos, R. C.; Hacon, S. de S.; Farias, R. A.; Caires, S. M. Mercury in Soils
394 and Sediments from Gold Mining Liabilities in Southern Amazonia. *Quím. Nova* **2007**, 30 (4).
395 <https://doi.org/10.1590/S0100-40422007000400003>.
396 (26)Wang, X.; Lin, C.-J.; Yuan, W.; Sommar, J.; Zhu, W.; Feng, X. Emission-Dominated Gas
397 Exchange of Elemental Mercury Vapor over Natural Surfaces in China. *Atmos. Chem. Phys.*
398 **2016**, 16 (17), 11125–11143. <https://doi.org/10.5194/acp-16-11125-2016>.
399 (27)Mazur, M.; Mitchell, C. P. J.; Eckley, C. S.; Eggert, S. L.; Kolka, R. K.; Sebestyen, S. D.; Swain,
400 E. B. Gaseous Mercury Fluxes from Forest Soils in Response to Forest Harvesting Intensity: A
401 Field Manipulation Experiment. *Science of The Total Environment* **2014**, 496, 678–687.
402 <https://doi.org/10.1016/j.scitotenv.2014.06.058>.
403 (28)Ma, M.; Wang, D.; Sun, R.; Shen, Y.; Huang, L. Gaseous Mercury Emissions from Subtropical
404 Forested and Open Field Soils in a National Nature Reserve, Southwest China. *Atmospheric*
405 *Environment* **2013**, 64, 116–123. <https://doi.org/10.1016/j.atmosenv.2012.09.038>.
406 (29)Eklöf, K.; Lidskog, R.; Bishop, K. Managing Swedish Forestry’s Impact on Mercury in Fish:
407 Defining the Impact and Mitigation Measures. *Ambio* **2016**, 45 (S2), 163–174.
408 <https://doi.org/10.1007/s13280-015-0752-7>.
409 (30)De Wit, H. A.; Granhus, A.; Lindholm, M.; Kainz, M. J.; Lin, Y.; Braaten, H. F. V.; Blaszcak, J.
410 Forest Harvest Effects on Mercury in Streams and Biota in Norwegian Boreal Catchments.
411 *Forest Ecology and Management* **2014**, 324, 52–63.
412 <https://doi.org/10.1016/j.foreco.2014.03.044>.
413 (31)Abraham, J.; Dowling, K.; Florentine, S. Effects of Prescribed Fire and Post-Fire Rainfall on
414 Mercury Mobilization and Subsequent Contamination Assessment in a Legacy Mine Site in
415 Victoria, Australia. *Chemosphere* **2018**, 190, 144–153.
416 <https://doi.org/10.1016/j.chemosphere.2017.09.117>.
417 (32)Howard, D.; Macsween, K.; Edwards, G. C.; Desservettaz, M.; Guérette, E.-A.; Paton-Walsh, C.;
418 Surawski, N. C.; Sullivan, A. L.; Weston, C.; Volkova, L.; Powell, J.; Keywood, M. D.; Reisen,
419 F.; (Mick) Meyer, C. P. Investigation of Mercury Emissions from Burning of Australian
420 Eucalypt Forest Surface Fuels Using a Combustion Wind Tunnel and Field Observations.
421 *Atmospheric Environment* **2019**, 202, 17–27. <https://doi.org/10.1016/j.atmosenv.2018.12.015>.
422 (33)Feinberg, A.; Dlamini, T.; Jiskra, M.; Shah, V.; Selin, N. E. Evaluating Atmospheric Mercury
423 (Hg) Uptake by Vegetation in a Chemistry-Transport Model. *Environ. Sci.: Processes Impacts*
424 **2022**, 24 (9), 1303–1318. <https://doi.org/10.1039/D2EM00032F>.
425 (34)Hurt, G. C.; Chini, L.; Sahajpal, R.; Frolking, S.; Bodirsky, B. L.; Calvin, K.; Doelman, J. C.;
426 Fisk, J.; Fujimori, S.; Klein Goldewijk, K.; Hasegawa, T.; Havlik, P.; Heinemann, A.;
427 Humpenöder, F.; Jungclaus, J.; Kaplan, J. O.; Kennedy, J.; Krisztin, T.; Lawrence, D.;
428 Lawrence, P.; Ma, L.; Mertz, O.; Pongratz, J.; Popp, A.; Poulter, B.; Riahi, K.; Shevliakova, E.;
429 Stehfest, E.; Thornton, P.; Tubiello, F. N.; van Vuuren, D. P.; Zhang, X. Harmonization of
430 Global Land Use Change and Management for the Period 850–2100 (LUH2) for CMIP6. *Geosci.*
431 *Model Dev.* **2020**, 13 (11), 5425–5464. <https://doi.org/10.5194/gmd-13-5425-2020>.
432 (35)Michelazzo, P. A. M.; Fostier, A. H.; Magarelli, G.; Santos, J. C.; de Carvalho, J. A. Mercury
433 Emissions from Forest Burning in Southern Amazon. *Geophys. Res. Lett.* **2010**, 37 (9), L09809.
434 <https://doi.org/10.1029/2009GL042220>.

- 435 (36)Melendez-Perez, J. J.; Fostier, A. H.; Carvalho, J. A.; Windmüller, C. C.; Santos, J. C.; Carpi, A.
436 Soil and Biomass Mercury Emissions during a Prescribed Fire in the Amazonian Rain Forest.
437 *Atmospheric Environment* **2014**, *96*, 415–422. <https://doi.org/10.1016/j.atmosenv.2014.06.032>.
- 438 (37)Soares-Filho, B. S.; Nepstad, D. C.; Curran, L. M.; Cerqueira, G. C.; Garcia, R. A.; Ramos, C. A.;
439 Voll, E.; McDonald, A.; Lefebvre, P.; Schlesinger, P. Modelling Conservation in the Amazon
440 Basin. *Nature* **2006**, *440* (7083), 520–523. <https://doi.org/10.1038/nature04389>.
- 441 (38)Roulet, M.; Lucotte, M.; Farella, N.; Serique, G.; Coelho, H.; Passos, S.; Mergler, D. Effects of
442 Recent Human Colonization on the Presence of Mercury in Amazonian Ecosystems. *Water Air*
443 *Soil Pollut.* **1999**, *112*, 297–313.
- 444 (39)Renard, K. G.; Foster, G. R.; Weesies, G. A.; McCool, D. K.; Yoder, D. C. Predicting Soil
445 Erosion by Water: A Guide to Conservation Planning with the Revised Universal Soil Loss
446 Equation (RUSLE). *Agriculture handbook* **1997**, *703*.
- 447 (40)Borrelli, P.; Robinson, D. A.; Panagos, P.; Lugato, E.; Yang, J. E.; Alewell, C.; Wuepper, D.;
448 Montanarella, L.; Ballabio, C. Land Use and Climate Change Impacts on Global Soil Erosion by
449 Water (2015-2070). *Proc. Natl. Acad. Sci. U.S.A.* **2020**, *117* (36), 21994–22001.
450 <https://doi.org/10.1073/pnas.2001403117>.
- 451 (41)Borrelli, P.; Robinson, D. A.; Fleischer, L. R.; Lugato, E.; Ballabio, C.; Alewell, C.; Meusburger,
452 K.; Modugno, S.; Schütt, B.; Ferro, V.; Bagarello, V.; Oost, K. V.; Montanarella, L.; Panagos, P.
453 An Assessment of the Global Impact of 21st Century Land Use Change on Soil Erosion. *Nat*
454 *Commun* **2017**, *8* (1), 2013. <https://doi.org/10.1038/s41467-017-02142-7>.
- 455 (42)Panagos, P.; Borrelli, P.; Meusburger, K.; Yu, B.; Klik, A.; Jae Lim, K.; Yang, J. E.; Ni, J.; Miao,
456 C.; Chattopadhyay, N.; Sadeghi, S. H.; Hazbavi, Z.; Zabihi, M.; Larionov, G. A.; Krasnov, S. F.;
457 Gorobets, A. V.; Levi, Y.; Erpul, G.; Birkel, C.; Hoyos, N.; Naipal, V.; Oliveira, P. T. S.;
458 Bonilla, C. A.; Meddi, M.; Nel, W.; Al Dashti, H.; Boni, M.; Diodato, N.; Van Oost, K.;
459 Nearing, M.; Ballabio, C. Global Rainfall Erosivity Assessment Based on High-Temporal
460 Resolution Rainfall Records. *Sci Rep* **2017**, *7* (1), 4175. [https://doi.org/10.1038/s41598-017-](https://doi.org/10.1038/s41598-017-04282-8)
461 [04282-8](https://doi.org/10.1038/s41598-017-04282-8).
- 462 (43)Hengl, T.; De Jesus, J. M.; MacMillan, R. A.; Batjes, N. H.; Heuvelink, G. B. M.; Ribeiro, E.;
463 Samuel-Rosa, A.; Kempen, B.; Leenaars, J. G. B.; Walsh, M. G.; Gonzalez, M. R. SoilGrids1km
464 — Global Soil Information Based on Automated Mapping. *PLoS ONE* **2014**, *9* (8), e105992.
465 <https://doi.org/10.1371/journal.pone.0105992>.
- 466 (44)Lugato, E.; Smith, P.; Borrelli, P.; Panagos, P.; Ballabio, C.; Orgiazzi, A.; Fernandez-Ugalde, O.;
467 Montanarella, L.; Jones, A. Soil Erosion Is Unlikely to Drive a Future Carbon Sink in Europe.
468 *Sci. Adv.* **2018**, *4* (11), eaau3523. <https://doi.org/10.1126/sciadv.aau3523>.
- 469 (45)Van Oost, K.; Quine, T. A.; Govers, G.; De Gryze, S.; Six, J.; Harden, J. W.; Ritchie, J. C.;
470 McCarty, G. W.; Heckrath, G.; Kosmas, C.; Giraldez, J. V.; Da Silva, J. R. M.; Merckx, R. The
471 Impact of Agricultural Soil Erosion on the Global Carbon Cycle. *Science* **2007**, *318* (5850), 626–
472 629. <https://doi.org/10.1126/science.1145724>.
- 473